Scaling of Detonation Velocity in Cylinder and Slab Geometries for Ideal, Insensitive and Non-Ideal Explosives

Scott I. Jackson†, and Mark Short

Shock and Detonation Physics Group, Los Alamos National Laboratory,
Los Alamos, NM 87544

Experiments were conducted to characterize the detonation phase-velocity dependence on charge thickness for two-dimensional detonation in condensed-phase explosive slabs of PBX 9501, PBX 9502, and ANFO. In combination with previous diameter-effect measurements from a cylindrical rate-stick geometry, these data permit examination of the relative scaling of detonation phase velocity between axisymmetric and two-dimensional detonation. We find that the ratio of cylinder radius (R) to slab thickness (T) at each detonation phase velocity (D_0) is such that $R(D_0)/T(D_0) < 1$. The variation in the $R(D_0)/T(D_0)$ scaling is investigated with two Detonation Shock Dynamics (DSD) models: a lower-order model relates the normal detonation velocity to local shock curvature, while a higher-order model includes the effect of front acceleration and transverse flow. The experimentally observed $R(D_0)/T(D_0)$ (< 1) scaling behavior for PBX 9501 and PBX 9502 is captured by the lower-order DSD theory, revealing that the variation in the scale factor is due to a difference in the slab and axisymmetric components of the curvature along the shock in the cylindrical geometry. The higher-order DSD theory is required to capture the observed $R(D_0)/T(D_0)$ (< 1) scaling behavior for ANFO. An asymptotic analysis of the lower-order DSD formulation describes the geometrical scaling of the detonation phase velocity between the cylinder and slab geometries as the detonation phase velocity approaches the Chapman-Jouguet value.

Key words:

---

1. Introduction

Condensed-phase explosives have long been known to exhibit a detonation velocity dependence with charge scale. Experiments in cylindrical and slab geometries have previously been used to study this effect and determine its dependence on both charge scale and shape. Despite these efforts, the physics governing the variation of detonation velocity for different geometries is not fully understood.

1.1. *The Size Effect*

The influence of charge size on detonation velocity in a high explosive (HE) is generally measured in cylinders of constant diameter. This "rate-stick" geometry generates a steady detonation when the cylinder is of sufficiently large aspect ratio. By performing tests at multiple diameters, it is observed that the explosive detonation velocity monotonically decreases with decreasing radius (Campbell & Engelke 1976), as shown in figure 1. This

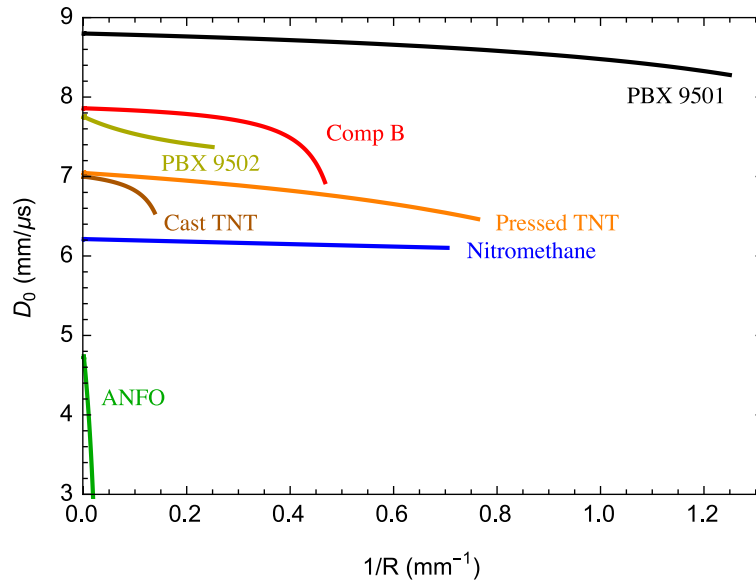† Email address for correspondence: sjackson@lanl.gov

FIGURE 1. The diameter effect for several high explosives with no confinement. Curves for PBX 9501, PBX 9502 and ANFO are from authors cited in Tables 3, 6, and 8, with others from Campbell & Engelke (1976).

diameter effect relationship is commonly plotted as axial detonation velocity (D_0) versus inverse charge radius ($1/R$). It is due to lateral expansion of high-pressure reaction zone gases, the pressure of which (ranging from a few GPa in non-ideal high explosives to a few tens of GPa in ideal high explosives) exceeds the strength of any confining material. The expansion leads to streamline divergence in the reaction zone and a curved detonation shock as shown in figure 2. The energy balance between the detonation shock and sonic plane influences the detonation speed (Bdzil 1981). As the charge radius decreases, increasing energy is lost to streamline divergence, while the curved sonic plane progresses towards decreasingly reacted states. These effects reduce the chemical energy available to drive the detonation shock, manifesting lower detonation velocities at smaller charges. There are two limiting cases; steady detonation propagation is not possible below a critical *failure diameter* $2R_c$, while for infinite radius charges, the flow is one-dimensional and the detonation propagates at the Chapman-Jouguet (CJ) detonation velocity.

The quantitative aspects of the diameter-effect curves, including their level of concavity and R_c, differ with explosive formulation, microstructure, and reaction kinetics. The sum of these effects cannot currently be predicted *a priori*. Despite this limitation, coarse classifications exist based on the relative lengths of each explosive's CJ detonation reaction zone and its diameter-effect variation over engineering scales. Ideal explosives, such as cyclo-tetramethylene-tetranitramine (HMX), have short reaction zone lengths of $\mathcal{O}(0.1 \text{ mm})$ and are observed to have small variations in detonation velocities from the CJ speed over a wide range of charge diameters. Insensitive high explosives, such as 2,4,6-triamino-1,3,5-trinitrobenzene (TATB), exhibit two disparately sized zones of heat release that combine for an overall reaction-zone size of $\mathcal{O}(1 \text{ mm})$, a more pronounced diameter effect (*i.e.* steeper slope on D_0 vs. R^{-1} plots), and a larger failure diameter. Non-ideal high explosives, such as prilled ammonium nitrate and fuel oil (ANFO), typically have reaction zone lengths on the scale of centimeters $\mathcal{O}(10 \text{ mm})$, very strong diameter effects, and very large failure diameters.
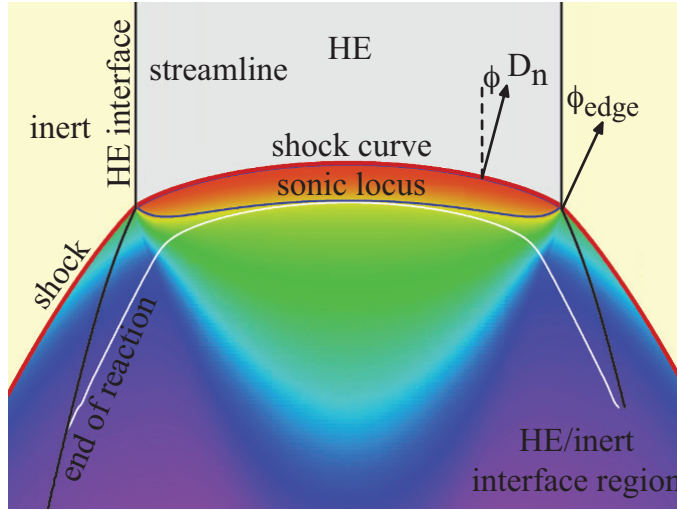
FIGURE 2. Curvature on the detonation shock induced by radial flow expansion into the reaction zone. Coloring of postshock flow indicates relative pressure, with low pressure flow as blue and high pressure flow as red. Figure adapted from Bdzil *et al.* (2003).

Rectangular slabs are sometimes used as a second fundamental geometry for analysis of detonation velocity with charge size. Slabs exhibit analogous behavior to rate sticks, but can be used to generate two-dimensional reaction zone flow (detailed in section 2). These slab reaction zones only laterally expand in the thickness dimension, in contrast to the two-dimensional (radial and azimuthal) expansion of the rate stick. Because of this geometric effect, less reaction zone energy is lost to flow divergence for a given slab thickness T as compared to a rate stick with equivalent radius $2R = T$ and, as a result, slabs exhibit a higher detonation velocity relative to comparably sized rate-sticks. While not explicitly named previously, we refer to the detonation velocity dependence with inverse slab thickness as the *thickness effect*, the combined diameter- and thickness-effect relationships as the *size effect*, and the critical slab thickness as T_c.

1.2. *Prior Scaling Measurements*

For a given HE, we define the *steady propagation scale factor* $R(D_0)/T(D_0)$ as a comparison of the rate-stick radius and slab thickness that give an identical detonation velocity in the two geometries (for the same confinement conditions), while the *critical scale factor* R_c/T_c represents the ratio of the critical radius and critical thickness in the cylinder and slab geometries respectively. Variation of these scale ratios for a variety of explosives, along with the implications for detonation dynamics in different geometries, has received much attention recently and forms the basis for the current paper. Previously measured scale factors for steady detonation propagation and failure are summarized in table 1. The scope of prior work is limited, with only nine formulations having been studied by four groups. These formulations span a range of detonation behavior from homogeneous liquids with relatively flat diameter-effect curves, to heterogeneous plastic-bonded explosives with moderately sloped diameter-effect curves, to non-ideal emulsion explosives with steep diameter-effect curves. Most of the studies were equipped with a witness plate diagnostic to measure R_c/T_c, while $R(D_0)/T(D_0)$ was only reported for three emulsion explosives. Additionally, most experiments did not monitor the detonation front for the occurrence of transverse instabilities, which have been observed to occur in liquid and liquid-emulsion explosives (Engelke & Bdzil 1983). The presence of such instabilities

Reference	$R(D_0)/T(D_0)$	R_c/T_c	Mixture	Geometry
Ramsay (1985)	NA	1.15	PBX 9502	UPT
Gois et $al.$ (1996)	NA	≈ 1	NM-PMMA-(2%, 3%)GMB	UPT
Gois et $al.$ (1996)	NA	1.6	NM-PMMA-(0.2%)GMB	UPT
Petel & Higgins (2006)	NA	1.6 ± 0.3	NM	C&S
Petel & Higgins (2006)	NA	1.8 ± 0.2	65%NM-35%NE	C&S
Petel et $al.$ (2006)	NA	1.55 ± 0.15	HN-HZ	C&S
Petel et $al.$ (2006)	NA	1.65 ± 0.15	NM-DETA-GB	C&S
Mack et $al.$ (2007)	NA	0.81 ± 0.15†	NM	A
Petel et $al.$ (2007)	NA	1.15 ± 0.05	65%NM-35%NE-GB	C&S
Petel et $al.$ (2007)	1.5–1.9	1.95 ± 0.45	APEX Elite emulsion	C&S
Silvestrov et $al.$ (2008)	1-1.1	1.225 ± 0.025	fine AN emulsion	C&S
Higgins (2009)	1-1.3	1.63 ± 0.04	NM-PMMA-(0.2%)GMB	C&A

TABLE 1. Summary of prior work. (AN = ammonium nitrate, DETA = diethylenetriamine, GB = glass beads, GMB = glass microballoons, HN = hydrazine nitrate, HZ = hydrazine, NM = nitromethane, NE = nitroethane. The geometries are UPT = unsteady prism test, C&S = cylinder and slab, A = annulus, C&A = cylinder and annulus). †This critical scale factor was calculated using the value of T_c calculated by Mack et $al.$ (2007) and R_c calculated by Petel & Higgins (2006).

would both alter the detonation physics from those described in section 1.1 and section 3 and also would likely affect any scale factor measurements.

Ramsay (1985) evaluated T_c of PBX 9502 under both confined and unconfined conditions using a "prism test," composed of a wedge-shaped cuboid of PBX 9502 initiated with a line wave generator (Jackson et $al.$ 2006; Morris et $al.$ 2009) at one trapezoidal face. A witness plate on the opposing face was dented if detonation successfully transited the wedge. The geometry was intended to evaluate a range of explosive thickness in a single test, as opposed to fielding multiple slab tests. At room temperature, Ramsay (1985) found a critical prism thickness of 3.8 mm. Comparison to cylindrical data of Campbell & Engelke (1976) yielded $R_c/T_c = 1.15$. Given the inherent unsteadiness of the test design, this value is likely an overestimate: Detonation will travel at a higher velocity in thicker regions of the wedge, overdriving and delaying incipient failure in adjacent thinner regions. Additionally, the short detonation run length (50 mm) may have been insufficient for the detonation to relax from any booster overdrive to steady propagation. For these reasons, Ramsay (1985) noted that the prism only provided only a preliminary estimate of T_c, which could be improved with constant-thickness slab tests.

Gois et $al.$ (1996) also performed prism tests to measure T_c for emulsion explosives composed of nitromethane (NM) with small concentrations of glass microballoons (GMBs) and dissolved PMMA. The dissolved PMMA sufficiently increases the mixture viscosity to suspend the GMBs, which increase the sensitivity of the mixture. They measured a critical scale ratio R_c/T_c close to unity for 2% and 3% GMB concentrations when compared to previous tests (Gois et $al.$ 1991) in the cylindrical geometry. For 3% GMB concentration $R_c/T_c < 1$, but for 2% GMB concentration $R_c/T_c > 1$. For 1% GMB concentration, $R_c/T_c \approx 0.7$, however, R_c/T_c abruptly increased to 1.6 for very low GMB concentrations of 0.2%. As with Ramsay (1985), Gois et $al.$ (1996) likely overestimate R_c/T_c due to the prism geometry.

Petel & Higgins (2006) report the critical radius and thickness of two liquid explosive mixtures, pure NM and a blend of 65% NM and 35% nitroethane (NE) by mass, under aluminium confinement. They measured R_c/T_c of 1.6 and 1.8 for the NM and NM/NE

mixtures, respectively. Note, however, that the detonation velocities of pure NM and NE are approximately 6.2 and 5.4 mm/μs, respectively (Engelke & Bdzil 1983; Yoshinaka & Zhang 2004), while the longitudinal sound speed of the confining aluminium alloy is 6.4 mm/μs. If the detonation velocity is lower than the confiner sound speed, the flow in the confiner becomes subsonic and shockless. Precursor waves in the confiner can then be driven ahead of the detonation (Sharpe & Bdzil 2006; Jackson *et al.* 2011; Short & Jackson 2015), potentially influencing both the detonation propagation speed and failure process (Short *et al.* 2010).

Mack *et al.* (2007) performed critical thickness experiments with pure NM in an annular channel confined by an inner aluminium rod and an outer aluminium tube. Mack *et al.* (2007) argue that for an annular channel thickness much less than the annular radius, the axisymmetric component of curvature is negligible. They measured a critical thickness of 1.45 ± 0.15 mm, a factor of two larger than their group's previous T_c measurement of 0.75 ± 0.1 mm. They proposed that Petel & Higgins (2006) may not have allowed the detonation to propagate a sufficiently long distance in either the slab or cylindrical geometries (> 10 aspect ratio) to quantify detonation failure. In addition, an estimate for the magnitude of the axisymmetric curvature component in the annulus was not given. A non-negligible axisymmetric curvature component could cause an increase in the calculated value of T_c relative to the 2D slab geometry. As with their previous study, precursor motion in the aluminium confiner may also be present. Using the R_c value for pure NM from Petel & Higgins (2006) with the new critical thickness $T_c = 1.45 ± 0.15$ mm gives a revised critical scale factor of $R_c/T_c = 0.81 ± 0.15$.

Petel *et al.* (2006, 2007) performed rate stick and slab tests with four explosive formulations: (1) a 65%NM–35%NE mixture sensitized with solid glass beads (GBs), (2) an ammonium nitrate and aluminium-flake based commercial blasting emulsion named Apex Elite manufactured by Orica Mining Services, (3) a NM mixture sensitized with diethylenetriamine (DETA) and GBs, and (4) a mixture of hydrazine nitrate (HN) and hydrazine (HZ). The slab geometry used by Petel *et al.* (2006, 2007) was similar to that used by Petel & Higgins (2006). Aluminium confinement was used for the NM-NE-GB and HN-HZ mixtures, while the NM-DETA-GB explosive was confined by glass, and Apex Elite confined by PMMA. While R_c/T_c was measured for all explosives, $R(D_0)/T(D_0)$ was only measured for Apex Elite. For the NM-NE-GB mixture, R_c/T_c was 1.15 ± 0.05. For the NM-DETA-GB mixture, R_c/T_c was 1.65 ± 0.15. For the HN-HZ mixture, R_c/T_c was 1.55 ± 0.15. For Apex Elite, R_c/T_c was 1.95 ± 0.45 while $R(D_0)/T(D_0)$ ranged from 1.5–1.9, the scale factor increasing as D_0 decreased.

Subsequently, Silvestrov *et al.* (2008) also performed rate sticks and slab tests with an ammonium-nitrate-based emulsion explosive. They measured $R_c/T_c = 1.225 ± 0.025$ and $R(D_0)/T(D_0) = 1$–1.1. Finally, Higgins (2009) evaluated the geometric scaling for the lowest GMB concentration (NM-PMMA-(0.2% wt.) GMB) mixture tested by Gois *et al.* (1991). The experimental geometries tested were cylindrical rate sticks and annular channels similar to that of Mack *et al.* (2007), but with PVC confinement. Higgins (2009) reported $R_c/T_c = 1.63 ± 0.04$ and $R(D_0)/T(D_0) = 1$–1.3.

Citing the correlation between detonation velocity and shock curvature that has long been observed (Bdzil 1981), Petel *et al.* (2006, 2007), Silvestrov *et al.* (2008) and Higgins (2009) suggest that curvature-based theories of detonation propagation and failure should predict scale factors where $R(D_0)/T(D_0) = 1$ and $R_c/T_c = 1$. Their conjecture is based on the geometric observation that detonation in a cylinder experiences two orthogonal components of reaction zone flow expansion, while detonation in a slab only expands along a single axis. With the assumption that all components experience equal curvature (which we address in section 3.1.2), they conclude that a cylinder and slab will have the same

total curvature and detonation velocity when $R = T$, hereafter referred to as the $R = T$ scaling. Scaling measurements deviating from unity (which encompasses essentially all existing size-effect data) were then attributed to factors other than curvature dominating the physics of detonation propagation and failure.

1.3. *Paper Outline*

We examine the variation of scale factor R/T for three characteristically different explosives by experimentally measuring their slab thickness effect (section 2). Prior cylindrical diameter-effect data are then used to find the experimentally observed scaling between these geometries. The experimental results are compared to predictions from two Detonation Shock Dynamics (DSD) models (section 3). A lower-order theory relates detonation velocity to front curvature, while a higher-order theory includes front acceleration and transverse flow terms. We show that lower-order theories are entirely consistent with the variable non-unity scale factors observed experimentally because the orthogonal curvature components in the rate stick are not, in general, equal. The higher-order theory is required to describe the R/T variation for ANFO. Finally, an asymptotic study is used to provide insight into the variation of the R/T scale factor for detonation velocities approaching the Chapman-Jouget limit (section 4).

2. Experiments

2.1. *Slab Test Geometry*

The rectangular slab configuration was initially proposed as a simple configuration to measure HE Gurney energy (Kennedy 1997), and has since been used to characterize interactions between explosives and various inert confiners (Eden & Wright 1965; Eden & Belcher 1989; Hill & Aslam 2004; Anderson *et al.* 2014). It was also used by Collyer *et al.* (1998) to measure thickness-effect curves and detonation shock shapes to derive a DSD calibration for the insensitive TATB based explosive EDC35 (95/5 TATB/Kel-F wt%).

In this study, slab geometry experiments were designed to generate a region of quasi-steady two-dimensional flow, in which detonation velocities and front shapes can be measured. The slabs in the current study have no confinement to match the previously obtained data on unconfined rate-sticks. An example of the slab configuration (for PBX 9502) is shown in figure 3. The experiments consist of a large-aspect-ratio rectangular-cuboid HE main charge that is initiated by a high-precision detonation line wave generator. For PBX 9502 and ANFO, the wave is then transmitted to a rectangular-cuboid booster charge that is composed of an explosive with sufficient output strength to promptly initiate a linear detonation wave in the adjacent main charge. The detonation then propagates along the main charge to the front-shape measurement surface located at the centerline (across the thinnest dimension T) of the output face. Time of arrival wires (or pins) track the phase velocity of the detonation along the charge centerline.

For a linear detonation input and a main charge of finite length, the charge will contain a region of two-dimensional flow as indicated in figure 3. The transition of the HE region to air at the sides of the charge creates rarefaction waves which propagate laterally into the HE rendering the following flow three-dimensional. Nominally, we expect the disturbance wavehead to propagate along the shock at the local sound speed of the shocked reactants. However, using a small resolved heat release model in a 2D configuration, Bdzil & Stewart (1986) showed that the propagation of a two-dimensional disturbance from the edge of a charge consisted of a two-wave hierarchy. The main disturbance is carried in a region of parabolic flow connected to the edge of the charge. The parabolic flow region
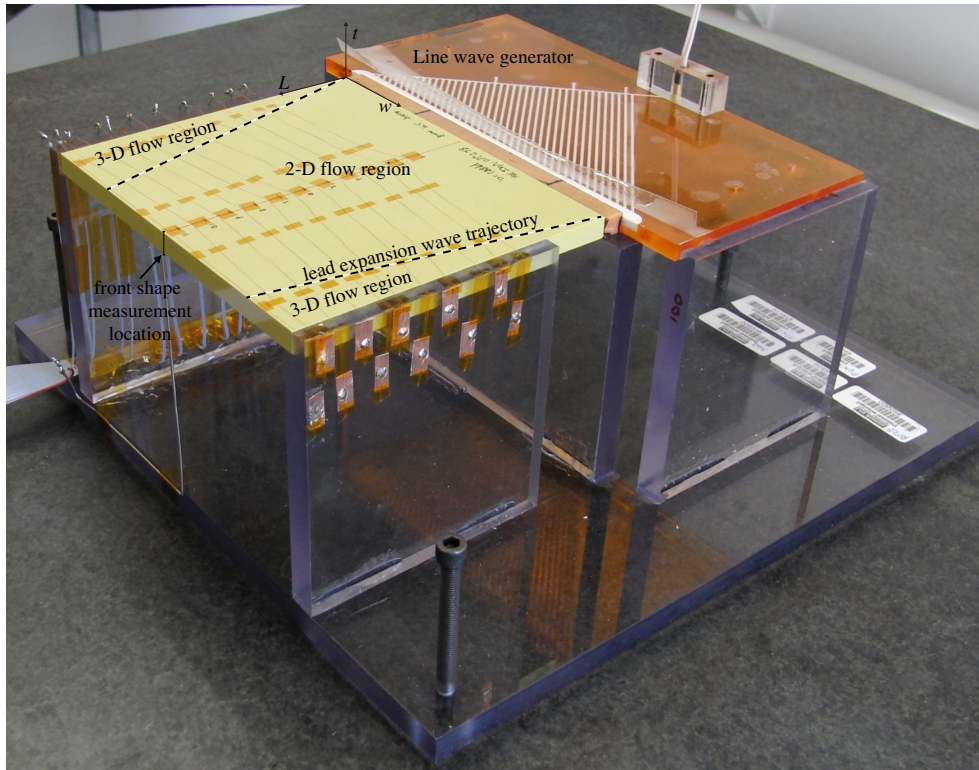
FIGURE 3. Test geometry for a PBX 9502 slab. The slab is initiated with a line wave generator and boosted by a rectangular cuboid of Composition B. The dashed lines are illustrative of the path of the wave head that propagates disturbances from the slab edges toward the slab center, rendering the following flow three-dimensional. A spatially decreasing region of two-dimensional flow remains in the center of the slab.

is connected to the region of one-dimensional undisturbed flow by a hyperbolic wave regime, whose wavehead amplitude is small. Consequently, significant modifications to the one-dimensional regime only occur with the arrival of the parabolic flow region. Bdzil & Davis (1975) contains a reference to unpublished experiments on unconfined Composition B rate-sticks that indicate the velocity of the laterally moving side rarefaction in the explosive is about 1/4 of the detonation velocity. This is consistent with the study by Bdzil & Stewart (1986). Jackson & Short (2012) for PBX 9502 and Chiquete *et al.* (2014) for PBX 9501 have also performed experiments and analysis that verified the presence of a large two-dimensional flow region at the downstream shock breakout surface for slab charges with similar aspect ratios to the present experiments. In the present work, main charge dimensions are selected such that a two-dimensional region is maintained over the time-of-arrival pin and front-shape measurement region.

The axial charge length in the direction of detonation propagation must also be sufficiently long that a steady two-dimensional detonation velocity can be achieved. Typically, this requires a length of several charge thicknesses (T) to both damp out any booster overdrive or underdrive and allow for the two-dimensional flow to be established. With a single exception (shot 8-1661), the experiments in this study had length-to-thickness ratios $L/T \geqslant 10$. Thus, charges had to be as long as possible to achieve a steady-state velocity and as wide as possible to maintain a sufficient two-dimensional measurement region. For less-ideal detonations with larger reaction zones, these two considerations

Shot Number	T (mm)	L (mm)	W (mm)	ρ_0 (g/cc)	D_0 (mm/μs)	$\pm SE$ (mm/μs)
8-1710	0.80	130.0	150.0	1.83	>7.73	0.14
8-1705	1.00	130.0	150.0	1.831	8.461	0.003
8-1701	1.98	130.0	150.0	1.8311	8.687	0.001
8-1595	3.00	135.0	151.2	1.832	8.738	0.006
8-1646	3.00	135.0	151.2	1.832	8.723	0.004
8-1691	3.00	135.0	151.2	1.8334	8.751	0.002
8-1694	3.99	130.0	150.0	1.8309	8.755	0.002
8-1723	6.00	130.0	150.0	1.8297	8.766	0.001
8-1735	8.01	130.1	150.1	1.8295	8.777	0.003

TABLE 2. PBX 9501 slab experiment dimensions and thickness effect data. Shots fired at 22.5±2.5°C. PBX 9501 lot was HOL89C730-010. Shot 8-1710 only indicates a minimum possible velocity due to nonplanar initiation, as described in the text. Densities were measured with multiple instruments, which yielded varying significant figures as shown.

require very large charges compared to more sensitive formulations (detonations are considered ideal when the wavefront radius of curvature is significantly larger than the reaction zone length: $1/\kappa >> \ell_{RZ}$). This will be apparent in the relative test dimensions of each formulation presented below.

2.2. *PBX 9501 Slab Experiments*

Nine slab experiments were performed with the PBX 9501 formulation. PBX 9501 is a polymer bonded explosive composed of 95.0 weight (wt.) % HMX explosive crystals bonded with a binder mixture of 2.5 wt. % Estane and a 2.5 wt. % eutectic mixture of bis(2,2-dinitropropyl)acetal and bis(2,2-dinitropropyl)formal (BDNPA/BDNPF). PBX 9501 is considered to be a conventional high explosive with a spatially small reaction zone of $\mathcal{O}(0.1 \text{ mm})$, a nominal detonation velocity D_0 of 8.8 mm/μs, and a critical radius near 0.76 mm (Gibbs & Popolato 1980).

PBX 9501 slab experiments were boosted with a line wave generator composed of XTX-8003 (80% PETN or pentaerythritol tetranitrate and 20% silicone resin, specifically Sylgard 182 elastomer). The line wave generator had an output width and thickness of 157 and 3.2 mm, respectively. Due to the high shock sensitivity of PBX 9501, no additional boosting charge was used. The PBX 9501 main charges were approximately 130 mm in length and 150 mm in width with thicknesses varying from 0.8–8.0 mm. Nominal densities were 1.83 g/cc. Specific dimensions and densities are listed in table 2.

Ionization probes were used as the time-of-arrival diagnostic for the PBX 9501 test series. Each ionization probe consisted of a 79.8-μm-diameter (40-AWG) copper wire that was located along the axial centerline of one face of the charge. The wires were bent into a chevron shape and oriented with the chevron tip along the axial charge centerline so that the detonation would first contact this tip. These wires were raised to an electrical potential of 75.0 V through use of an RC circuit. A single, thicker copper grounding wire was located on the axial centerline of the opposing charge surface. Arrival of the ionization front associated with the detonation wave at each probe allowed current to flow from the high-voltage wire to ground, resulting in a measured voltage drop across the resistor in the RC circuit. Probe locations were measured to better than 30 μm and the pin voltage was sampled with a bandwidth of 1 GHz (5 GS/s sample rate) during each test.

For each test, either 11 or 22 ionization probes were used on the main charge. The

Shot Number	R (mm)	$L/Dia.$ (mm)	ρ_0 (g/cc)	D_0 (mm/μs)	$\pm SE$ (mm/μs)
8-706[††]	20.75	N/A	1.832	8.786	0.0004
8-707[*]	20.75	N/A	1.831	8.777	0.0004
8-800[†]	20.65	N/A	1.838	8.810	0.0004
8-888[†††]	20.65	N/A	1.835	8.790	0.0009
8-889[†]	20.65	N/A	1.836	8.794	0.0005
15-2781	20.65	N/A	1.838	8.793	0.002
C-4431	12.7	>10	1.832	8.790	0.001
C-4442	2.505	>10	1.832	8.722	0.002
C-4427	1.415	>10	1.832	8.612	0.011
N/A	1.415	N/A	1.828	8.618	0.015
C-4440	1.005	>10	1.832	8.487	0.013
C-4441	0.79	>10	1.832	8.259	0.013

TABLE 3. PBX 9501 diameter-effect data for cylindrical rate-sticks. Data points are taken from a recent compilation by Hill (2012). Shots conducted approximately at room temperature. [*]PBX 9501 lot RON00H144-001. [†]PBX 9501 lot BAE02D145-004. [††]PBX 9501 lot HOL89C730-010. [†††]PBX 9501 lot BAE03L145-007. For all other shots, the lot specification was not available. Shots 8-706 and 8-707 had associated front curvature measurements (Hill 2012). N/A= record not available.

first probe was located 30 mm from the upstream (initiating) end of the PBX 9501 charge. Subsequent probes were equidistantly spaced over the remaining distance to the downstream end of the charge, resulting in probe separation spacings of 9.1 mm. Probe position and detonation arrival time data were fitted to a line using a least-squares fit optimization. The slope of the line was the steady-state detonation velocity D_0. These velocities are reported in table 2 along with the standard error (SE) associated with the fit to D_0.

As expected, the detonation velocity is seen to increase with slab thickness. Excepting a single abnormally initiated test (described below), standard error values are all less than ± 0.006 mm/μs or 0.07% D_0, indicating that the detonation velocity is steady. The three repeat shots performed at an identical thickness of 3.00 mm exhibit a velocity range of 0.028 mm/μs or 0.3% D_0. This range was likely influenced by charge density variations, which were present in the experiments.

The 0.8-mm-thick slab was inadequately boosted by the line wave generator and only initiated at one corner. The resulting detonation expanded cylindrically across the charge. The D_0 value listed in table 2 was inferred from a series of framing camera images of the experiment, substantially increasing the SE uncertainty relative to the ionization pin diagnostic. This result indicates that (1) the planar detonation velocity would have likely exceeded this cylindrically diverging detonation velocity and (2) the 0.8-mm-thick slab required a stronger booster for successful initiation.

Table 3 contains historical data from rate stick experiments in the cylindrical geometry that were recently compiled by Hill (2012). The cylindrical and slab rate stick data are plotted against each other in figure 4. The horizontal axis represents inverse charge radius $1/R$ or thickness $1/T$ so that the two geometries will overlay if the $R = T$ scaling, discussed in section 1, is satisfied. The data points indicate each experimental measurement. The curves shown were fit to the experimental data using a modified form of the

Formulation	Geometry	D_∞	A	R_1
PBX 9501	Cylinder	8.800	0.0191	0.4780
PBX 9501	Slab	8.800	0.0183	0.5251
PBX 9502	Cylinder	7.755	0.3979	-4.045
PBX 9502	Slab	7.755	0.4110	-2.909
ANFO	Cylinder	4.800	12.66	19.56
ANFO	Slab	4.800	24.02	7.579

TABLE 4. Parameters for the modified Eyring fitting form curves (2.1).

empirical Eyring equation (Campbell & Engelke 1976),

$$D_0(\ell) = D_\infty \left(1 - \frac{A}{\ell - R_1} \right), \tag{2.1}$$

where D_∞ (the CJ detonation velocity), A and R_1 are fitting parameters. Variable ℓ either represents the cylinder radius R or the slab thickness T. For fitting to the slab thickness effect and rate-stick diameter-effect PBX 9501 data in tables 2 and 3, D_∞ is fixed for both geometries based on estimates of D_{CJ} for PBX 9501 obtained previously at Los Alamos National Laboratory. The parameters A and R_1 are then fitted using a least squares approximation. PBX 9501 parameters for (2.1) are listed in table 4. Figure 4 shows the diameter- and thickness-effect curves resulting from the modified Eyring fitting form. Overall, the experimental PBX 9501 data is reasonably approximated by the $R = T$ scaling over the range of test conditions. For thicker charges ($R > 1.25$ mm and $T > 1.25$ mm) and higher detonation velocities ($D_0 > 8.55$ mm/μs), the agreement between the two geometries is excellent. Deviations only exist for the smallest (1.0 mm) slab that was properly initiated, where the detonation flow is less ideal due to increasing lateral expansion losses and lengthening reaction zone widths.

2.3. *PBX 9502 Slab Experiments*

Nine slab experiments were performed with PBX 9502. PBX 9502 is a plastic-bonded explosive composed of 95.0 wt. % TATB explosive bonded with 5.0 wt. % Kel-F 800, which is a a proprietary name for the thermoplastic chlorofluoropolymer Polychlorotri-fluoroethylene or PCTFE (Gibbs & Popolato 1980). PBX 9502 is an insensitive high explosive with a nominal detonation velocity of 7.8 mm/μs, and a failure diameter near 8.0 mm. The PBX 9502 reaction zone structure is considered moderate in spatial scale, exhibiting both fast reactions that are of $\mathcal{O}(0.1$ mm) and slower reactions of $\mathcal{O}(1.0$ mm).

PBX 9502 slab experiments were boosted with segments of Composition B formed in rectangular cuboids that were 8.0-mm long × 150-mm wide with a thickness equivalent to that of the PBX 9502 main charge. The Composition B charge was detonated by the same type of line wave generator used in the PBX 9501 tests. The PBX 9502 main charges were 127–150 mm in length and 150 mm in width, with thicknesses varying from 3.5–16.0 mm. Nominal densities were 1.87 g/cc. Specific dimensions are listed in table 5.

The ionization probes and velocity reduction methodology used with the PBX 9502 test series were identical in design to those used for the PBX 9501 tests. Inter-probe spacings were also equivalent. The distance of the first probe from the upstream end of the main charge varied with charge length. For charges 127-130 mm in length, this distance was 30 mm. For charges 150 mm in length, it was 50 mm.

As with the PBX 9501 data, the PBX 9502 detonation velocity increases with both slab thickness and slab initial density. Standard error values are all less than ±0.005 mm/μs
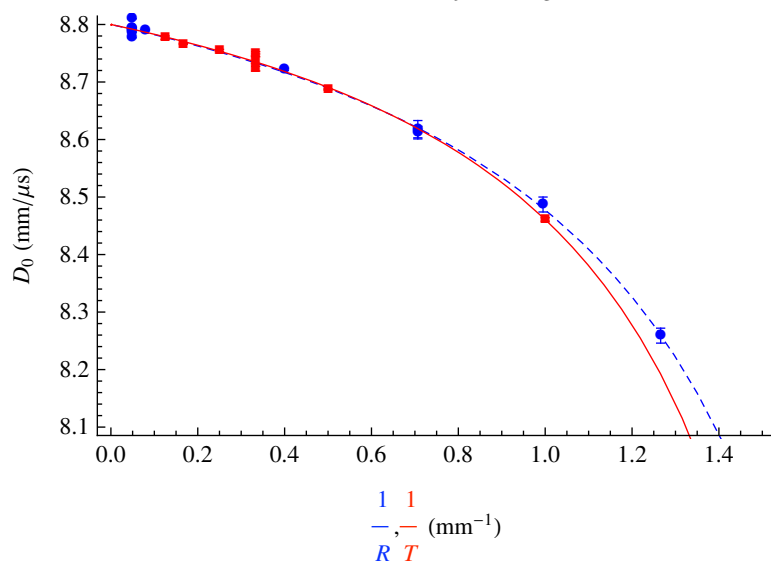
FIGURE 4. Size-effect data for PBX 9501. Blue circles ● and red squares ■ denote experimental cylindrical rate stick and slab test detonation velocities from tables 2 and 3. Blue dashed and red solid lines are modified Eyring-form fits to the cylindrical and slab experimental data, respectively. Error bars are plotted for each symbol, but may be smaller than the symbol.

Shot Number	T (mm)	L (mm)	W (mm)	ρ_0 (g/cc)	D_0 (mm/μs)	$\pm SE$ (mm/μs)	$D_{0,corr}$ (mm/μs)
8-1803	3.51	129.9	150.0	1.8741	Failed	N/A	Failed
8-1802	3.78	129.9	150.1	1.8740	7.237	0.002	7.266
8-1648	4.00	130.0	150.0	1.8741	7.262	0.002	7.291
8-1649	6.00	130.0	150.0	1.8738	7.391	0.004	7.421
8-1662	8.00	130.0	150.0	1.8741	7.439	0.002	7.468
PRAD-361	8.00	127.0	152.4	N/A	7.467	0.029	N/A
8-1589	8.00	127.0	151.1	1.8788	7.450	0.005	7.467
8-1590	8.00	127.0	151.1	1.8894	7.476	0.001	7.468
8-1647	12.00	150.0	150.0	1.8737	7.505	0.002	7.534
8-1661	16.00	150.0	150.0	1.8740	7.526	0.034	7.555

TABLE 5. PBX 9502 slab experiment dimensions and thickness-effect data. All slabs were manufactured from lot 008 material. Shots fired at 22.5±2.5°C. Data for PRAD-361 is from Aslam *et al.* (2009). D_0 is the experimentally measured detonation velocity. $D_{0,corr}$ is the detonation velocity after correction to an initial charge density of 1.886 g/cc.

or 0.07% of D_0, indicating that the detonation velocity is steady. The three repeat shots performed at an identical thickness of 8.00 mm exhibit a velocity range of 0.037 mm/μs or 0.5% of D_0 that, as discussed below, is dependent on the density of each charge. Framing camera images indicate that the 3.50-mm-thick charge was properly boosted, but failed a short distance downstream, indicating that the PBX 9502 slab was not able to support 2D detonation at this thickness.

2.3.1. *PBX 9502 Density-Adjusted Velocities*

The PBX 9502 data in table 5 exhibit a range of density variation that is four times larger than that present in the PBX 9501 data ($\Delta\rho_{9502} = 0.0157$ g/cc versus $\Delta\rho_{9501} =$
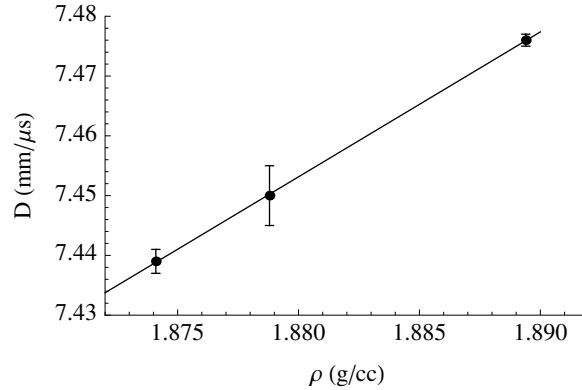
FIGURE 5. Experimental detonation velocity versus charge density for three shots with a thickness of 8.0 mm: 8-1662, 8-1589 and 8-1590.

Shot Number	R (mm)	$L/Dia.$ (mm)	ρ_0 (g/cc)	D_0 (mm/μs)	$\pm SE$ (mm/μs)
15-2839	25.0	N/A	1.886	7.641	N/A
15-2529	9.0	N/A	1.886	7.523	N/A
15-2844	9.0	N/A	1.886	7.512	N/A
8-1620	8	9.8	N/A	7.506	0.026
15-2851	5.0	N/A	1.890	7.421	N/A
8-1167	4.25	35.86	1.894	7.375	0.047
8-1159	4.00	38.10	1.893	Detonated	N/A
8-1169	3.75	40.64	1.894	Failed	N/A

TABLE 6. PBX 9502 diameter effect for cylindrical rate-sticks of PBX 9502 (lot 008). Shots fired at 22.5±2.5°C. Data for shots 15-2839, 15-2529, 15-2844 and 15-2851 are taken from Hill *et al.* (2006). Data for shots 8-1159, 8-1167, 8-1169 and 8-1620 are from diagnostics tests conducted by the present authors at Los Alamos National Laboratory in 2008 and 2012. Test 8-1159 only used a witness plate to evaluate failure and did not measure velocity due to failure of the ionization diagnostic.

0.0035 g/cc). These variations can have a significant effect on the detonation velocity for each test, making it worthwhile to correct for them. Initial explosive density affects the detonation velocity by varying the available energy release per unit volume of explosive. The exact way in which the diameter- and thickness-effect curves vary with initial charge density is unknown and likely depends nonlinearly on charge geometry and scale. To leading order, however, we assume a linear relationship between charge density and detonation velocity. The three 8.0-mm-thick slab rate sticks 8-1589, 8-1590 and 8-1662 allow determination of this relationship for the PBX 9502 slab tests. Figure 5 plots the detonation velocity versus charge density for these tests. A linear least-squares fit to the three data points yields $D_0 = 2.424\rho + 2.896$ with a standard error of 0.026 (mm/μs)/(g/cc) associated with the linear slope. (Performing a similar fit across all tests except the 16-mm one yields a value of 2.52 (mm/μs)/(g/cc.)) The linear slope of 2.424 (mm/μs)/(g/cc) can be used to adjust the experimentally measured detonation velocities to the expected velocity at a uniform density. In the last column of table 5, we report detonation velocities corrected to a density value of 1.886 g/cc as $D_{0,corr}$.
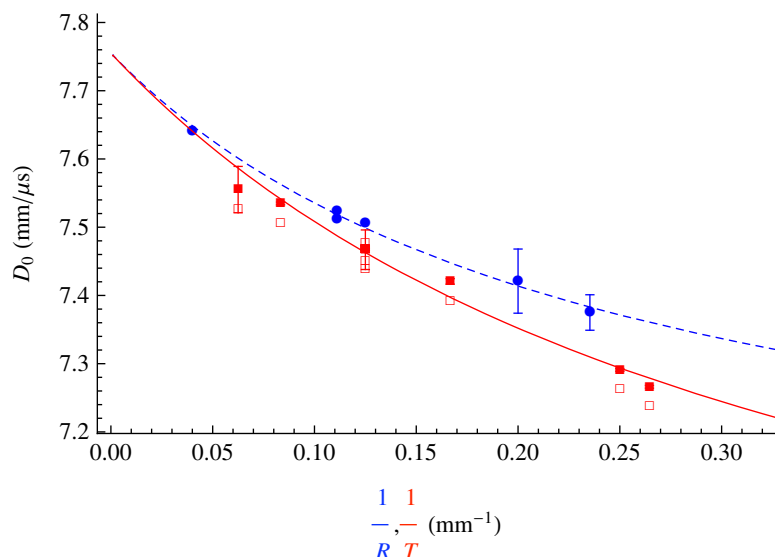
FIGURE 6. Size-effect data for PBX 9502. Blue circles ● are cylindrical rate stick detonation velocities (table 6). Open □ and filled red squares ■ denote experimental and density-corrected detonation velocities from the slabs, respectively (table 5). Blue dashed and red solid lines are the modified Eyring-form fits to the cylindrical and density-corrected slab experimental data, respectively. Error bars are plotted for the data with filled symbols using SE values from tables 5 and 6, but may be smaller than the symbol size.

2.3.2. *PBX 9502 Size-Effect Scaling*

Table 6 contains prior data from the cylindrical rate sticks experiments fielded with an identical PBX 9502 explosive lot (008) used in the present slab tests. The data indicate a critical radius between 3.75–4.00 mm, while table 5 indicates a critical thickness between 3.50–3.75. Thus, at failure, R/T is between 1.00-1.14 and consistent with our analysis (section 1) of the prism tests by Ramsay (1985). Figure 6 compares the diameter- and thickness-effect curves. As with the PBX 9501 data, the curves result from the fit of (2.1) to the experimental data. The density-corrected slab data was used in the curve-fitting process and fit parameters are given in table 4. The experimental PBX 9502 scale-effect data does not correspond well to the $R = T$ scaling over the range of conditions tested. The detonation velocity points for the slab geometry are consistently below those of the the cylindrical rate sticks and the deviation between the two increases as the charge size decreases. Specifically, the experimentally observed R/T ratio is near 0.83 and consistently below a value of unity.

2.4. *ANFO*

Unlike PBX 9501 and PBX 9502, ANFO detonation does not occur due to decomposition of a metastable molecule. Instead, ANFO is a heterogenous mixture of a hydrocarbon-based fuel oil (FO) and ammonium nitrate (AN) oxidizing agent that remains molecularly distinct at typical atmospheric temperatures. Shock loading mechanically mixes and ionizes these two components sufficiently to support the detonation reaction. The heterogenous nature of the mixture results in a very insensitive explosive (technically classified as a blasting agent) with a long spatial reaction zone of $\mathcal{O}(10 \text{ mm})$ and a failure diameter near 75 mm. Due to the nonideal nature of the explosive, the detonation velocity is sensitive to reaction zone flow divergence and experimentally observed veloci-

Shot	T	L	W	ρ_0	D_0	$\pm SE$
Number	(mm)	(mm)	(mm)	(g/cc)	(mm/μs)	(mm/μs)
EMRTC-6-2011	50.8	762.0	660.4	0.929	2.151	0.031
EMRTC-8-2011	76.2	1143.0	965.2	0.885	3.027	0.014
EMRTC-9-2011	101.6	1524.0	1270.0	0.870	3.661	0.008

TABLE 7. ANFO thickness effect in a slab geometry for a mass composition of 94% ammonium nitrate (Dyno Nobel explosive grade) and 6% No. 2 diesel fuel oil. Shots fired at ambient temperature.

ties range from 1.5–4.0 mm/μs, depending on charge size and confinement. A large range of detonation velocity variation is characteristic of non-ideal explosives.

Three slab experiments were performed with a standard ANFO formulation composed of 94 wt. % ammonium nitrate prills mixed with 6 wt. % No. 2 diesel fuel. Porous, explosive-grade ammonium nitrate was used from Dyno Nobel with a typical bulk density of 0.80 g/cc and an average prill diameter ranging from 1.4–2.0 mm. Mixing was accomplished by combining the prills and diesel fuel in a rotating barrel mixer for a minimum of 15 minutes. Unlike the PBX 9501 and PBX 9502 slab experiments, which were unconfined, the granular nature of ANFO required confinement to form a main charge. Rectangular forms were constructed of 3/4-inch-thick plywood for this purpose as a shock polar analysis indicates that plywood does not provide any effective confinement for ANFO detonation (Bdzil *et al.* 2002). After mixing, ANFO was then poured into each experimental assembly in 1-kg increments. Each incremental fill was hand-tamped to prevent significant clumping or void formation. This methodology was sufficient to achieve an ANFO density of 0.87–0.93 g/cc. The main charge was initiated by a booster charge and line wave generator composed of PETN-based sheet explosive. The booster charge width and thickness matched those of the adjacent main charge, while the booster length was approximately equal to the main charge thickness. The line wave generator thickness was 12 mm. Slab thicknesses of 50.8, 76.2 and 101.6 mm were fielded. Specific dimensions are listed in table 7. Shorting pins (Model CA-1038 from Dynasen, Inc.) were used for detonation time-of-arrival measurements. For the ANFO slab tests, the distance to the first shorting pin from the upstream end of the main charge was three charge thicknesses. A total of 11 shorting pins were used for each test. The probes were equally spaced over the remaining charge length, corresponding to inter-pin spacings of 38.1, 57.15, and 76.2 mm for the 50.8, 76.2 and 101.6 mm thick tests, respectively.

Detonation velocities are reported in table 7. The ANFO detonation velocity is seen to increase with the slab thickness. Standard error values range from 0.008–0.031 mm/μs (0.2–1.4%) and decrease with increasing slab thickness. Examination of the fit lines against the discrete time-of-arrival points for these tests indicate that the detonation is initially overdriven off the booster and decays as it propagates. We conjecture that the wave required more distance to decay to the lower steady detonation velocities measured in the thinner slabs, which resulted in higher standard error.

Table 8 contains previously published cylindrical rate-stick data for ANFO from Bdzil *et al.* (2002) that were performed with cardboard confinement, which provides a similar explosive-confined impedance match as the plywood used in the present ANFO slab tests. Figure 7 compares the diameter- and thickness-effect curves for ANFO using experimental data from tables 7, 8, and curves based on (2.1) with fit parameters from table 4. The experimental ANFO size-effect data does not correspond well to the $R = T$ scaling over the range of conditions tested. The detonation velocity points for the slab geometry are

Shot Number	Radius (mm)	L/Dia.	D_0 (mm/μs)	Density (g/cc)
4514	102.5	10	4.12	0.88
4408	76.5	10	3.68	0.88
4409	76.5	10	3.75	0.88
4407	64.0	10	3.40	0.88
4592	64.0	10	3.33	0.88
4406	64.0	10	3.36	0.88
4405	57.5	10	3.30	0.88
4400	51.0	10	2.97	0.88
4591	51.0	10	2.95	0.88
N/A	51.0	10	2.90	0.88
N/A	45.0	10	2.43	0.88
4403	45.0	10	2.45	0.88
N/A	38.5	10	1.63	0.88
N/A	38.5	10	1.47	0.88

TABLE 8. ANFO cylindrical rate-stick diameter effect for a mass composition of 94% ammonium nitrate and 6% No. 2 diesel fuel oil. Shots were performed at ambient temperature with Titan Energy explosive-grade AN. Standard errors are not available. Test series as described in Bdzil *et al.* (2002), with quantitative values of D_0 against radius supplied to the authors by Larry Hill.
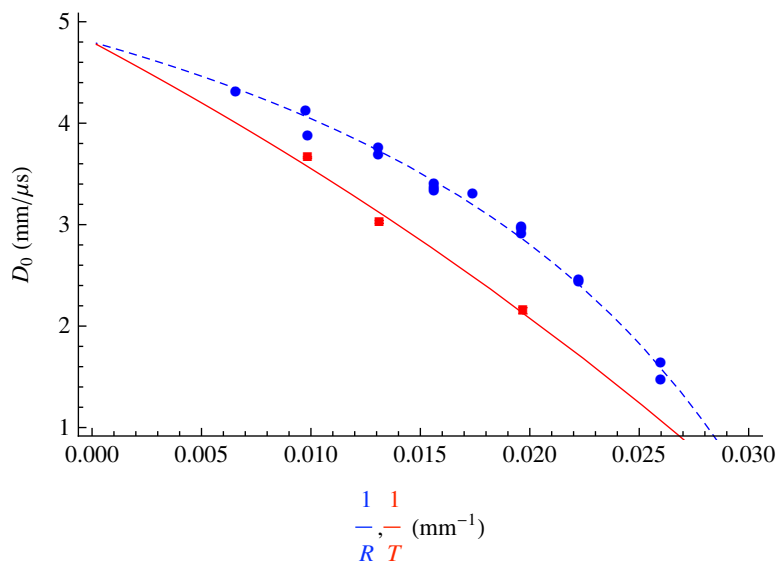
FIGURE 7. Size-effect data for ANFO. Red squares ■ and blue circles ● denote experimental slab and cylindrical geometry detonation velocities from tables 7 and 8. Blue dashed and red solid lines are modified Eyring-form fits to the cylindrical and slab experimental data, respectively. Error bars are plotted for the slab data only and may be smaller than the ■ symbol.

consistently below those of the cylindrical rate sticks. Specifically, the experimentally observed R/T ratio is near 0.7 and consistently below a value of 1.

2.5. *Measured Scale Factor R/T for Common D_0*

The modified Eyring-form fits can be used to evaluate the evolution of the R/T scaling inferred from experiment. Figure 8 plots the ratio of R to T using values derived from (2.1) and table 4 for common values of D_0. The black, orange and green curves indicate PBX
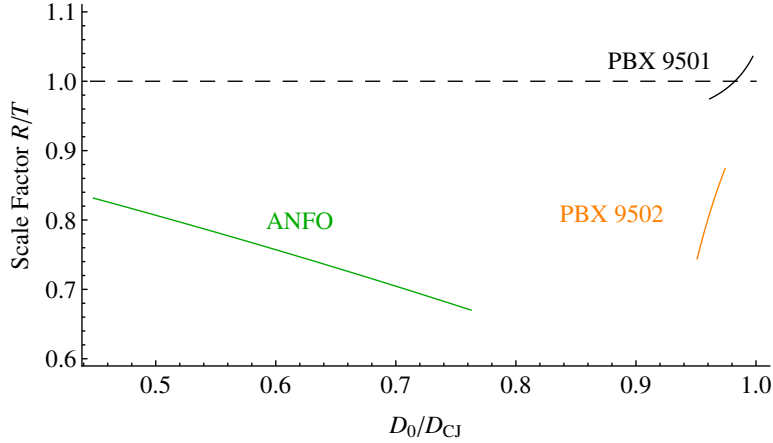
FIGURE 8. The ratio $R(D_0)/T(D_0)$ for PBX 9501, PBX 9502, and ANFO.

9501, PBX 9502, and ANFO, respectively. Extrapolation is avoided and each curve only spans the experimentally observed range of D_0 from tables 2, 5, and 7. The detonation velocity D_0 is normalized by D_{CJ}, which is taken as 8.8, 7.755, 4.8 mm/μs for PBX 9501, PBX 9502 and ANFO, respectively. PBX 9501 is seen to increase from $R/T = 0.974$–1.036 for $D_0/D_{CJ} = 0.961$–0.997. (Note that for larger D_0, the limited fitting parameters in (2.1) prevent an accurate determination of the variation of the R/T scale close to the CJ value. A more sophisticated DSD fitting form (Aslam 2007) applied to the rate-stick data alone gives a scale factor $R/T < 1$ at the larger phase velocities.) PBX 9502 ranges from $R/T = 0.744$–0.874 over $D_0/D_{CJ} = 0.951$–0.974. Finally, ANFO ranges from $R/T = 0.670$–0.832 for $D_0/D_{CJ} = 0.448$–0.763. Averaging over the interpolated region for each formulation gives average R/T values of 0.998, 0.813, and 0.753 for PBX 9501, PBX 9502, and ANFO, respectively. Thus, the R/T ratio is seen to decrease from unity as the explosive formulation becomes less ideal. Additionally, the PBX 9501 and PBX 9502 R/T values each individually decrease from unity as D_0 decreases. In contrast, the ANFO R/T values increase towards unity as D_0 decreases. In the following section, DSD is used to further understand the relationship between the thickness- and diameter-effect curves in the slab and rate-stick geometries for PBX 9501, PBX 9502 and ANFO.

3. Detonation Shock Dynamics

Detonation Shock Dynamics (or DSD) is an intrinsic surface propagation concept that replaces the detonation shock and reaction zone with a surface that evolves according to a prescribed intrinsic surface evolution law. Developed by Bdzil and Stewart (Bdzil & Stewart 1986; Stewart & Bdzil 1988*a*,*b*; Bdzil & Stewart 1989; Bdzil *et al.* 1989), it provides an advanced capability to describe detonation wave sweep through an arbitrarily complex geometry. There are two assumptions that underpin the DSD concept. The first is that the detonation shock front evolves quasi-steadily, i.e. the transit time of a particle through a characteristic reaction zone thickness is short compared to the temporal scale of changes in the shock shape. Secondly, the local curvature of the shock is small compared with the inverse of the characteristic reaction zone thickness. With these assumptions, at leading-order, the motion of the DSD surface relates the normal velocity of the surface (D_n) to the local surface curvature (κ). For the purposes of this paper, we refer to this as *lower-order* DSD. Higher-order effects, which account for the effects of front acceleration

and transverse flow, can be introduced in a systematic way. We refer to the inclusion of such terms in the DSD evolution laws as *higher-order* DSD.

3.1. *Lower-order DSD*

For the lower-order DSD theory, we define the existence of a general surface (DSD) propagation law given by

$$\kappa = f(D_n), \qquad (3.1)$$

for some arbitrary function f of D_n. The curvature κ represents the sum of the principal curvatures for any three-dimensional surface. In order to determine the evolution law (3.1) for a given HE, a specified functional form for f is assumed, and the functional form parameters are fitted to the shock shapes and diameter-effect curve obtained from experiments. This is typically done using the rate-stick geometry. In the rate-stick configuration, the DSD surface curvature has two components; the *slab* component, which is the two-dimensional curvature along a diameter of the rate-stick, and the corresponding *axisymmetric* component. The slab curvature component is determined by measuring the shock breakout times along a cylinder diameter at the end of the charge via a streak camera and mirror destruction (or turning) technique (Hill *et al.* 2006). Experimental calibration of lower-order DSD relations has been obtained for a variety of explosives including PBX 9501 (Aslam 2007), PBX 9502 (Bdzil 2003; Hill & Aslam 2010) and ANFO (Bdzil *et al.* 2002; Bdzil 2008). In particular, we note that for these explosives in an unconfined rate-stick geometry, the slab component of curvature has the property that it increases monotonically with increases in the radial coordinate from the cylinder axis.

For a given DSD form, determination of the surface motion also requires information on how the HE is confined. This is done at the HE/material interface through specification of the "edge" angle between the shock normal direction and the tangent to the material interface, which reflects the degree of HE confinement (Bdzil & Stewart 2007). Note that in the lower-order DSD theory, since D_n is a function of curvature, the different $D_n - \kappa$ curves obtained in rate-sticks of different radii (or slabs of different thicknesses) should overlap where there are common curvature points and ultimately combine to form a single curve in $D_n - \kappa$ space. Close grouping of such $D_n - \kappa$ curves have been observed for PBX 9501 (Chiquete *et al.* 2014) and PBX 9502 (Hill & Aslam 2010), but not for ANFO (Bdzil *et al.* 2002). We emphasize that the relation (3.1) is an intrinsic, coordinate-free surface propagation law. Thus, a given HE calibrated in one geometry, e.g. the cylindrical rate-stick, should be able to accurately reproduce detonation propagation dynamics in other geometries, such as the slab geometry considered here.

As noted above, Petel *et al.* (2006, 2007), Silvestrov *et al.* (2008) and Higgins (2009) proposed that curvature-based theories of detonation propagation and failure should have resulted in the recovery of scale factors where $R(D_0)/T(D_0) = 1$ and $R_c/T_c = 1$. Consequently, with the size-effect and failure scale factors in their experiments showing deviations away from unity, they surmised that other factors are contributing significantly to the physics of detonation propagation and failure in addition to curvature. The curvature-based lower-order DSD model (3.1), though, is able to dissociate contributions made from the axisymmetric and slab curvature components in a rate-stick configuration. These two components are generally not equal, except on the rate-stick axis, and thus we generally would not expect a steady propagation scale factor $R(D_0)/T(D_0) = 1$. In fact, we show in section 3.1.2 that any detonation whose propagation can be adequately represented by (3.1) must necessarily have a scale factor $R/T < 1$, provided that the slab component of curvature increases monotonically with radius.

Bdzil (1981) has shown that the scale factor $R(D_0)/T(D_0) = 1$ can be approached in

the limit where the streamline angle deflection behind the detonation shock is small. Thus for example, heavily confined explosives are more likely to limit to the small streamline deflection case of $R(D_0)/T(D_0) = 1$ (see section 4). For larger streamline deflection angles, Bdzil (1981) showed that the diameter- and thickness-effect curves diverge, where, for the specific reaction rate model used, it was found that $R(D_0)/T(D_0) < 1$. This result is consistent with the analysis in this paper.

While DSD based theories should be expected to capture the propagation scale factor $R(D_0)/T(D_0)$ across a range of explosives, DSD (lower- or higher-order) should not be expected to accurately determine the ratio of the critical diameter to thickness. The detonation failure process is inherently unsteady and involves significant increases in the characteristic reaction zone thickness. Additionally, there is no prior evidence that a purely curvature-based theory should predict failure. Thus we do not examine the critical diameter to thickness ratio further, and restrict our attention to examination of the steady propagation scale factor $R(D_0)/T(D_0)$.

3.1.1. *Lower-order DSD: Steady Propagation in Rate-Stick and Slab Geometries*

Consider the steady propagation of an axisymmetric detonation in the positive axial z direction of a cylindrical explosive, where the DSD surface is given as a function of radial coordinate r by $z = z_s(r)$, with a surface normal orientated in the direction of fresh reactants. Defining a level set function $S = z - z_s(r)$, the normal to the surface is

$$\mathbf{n} = \frac{\nabla S}{|\nabla S|} = \frac{1}{\sqrt{1 + [d(z_s(r))/dr]^2}} \left(-\frac{d}{dr} z_s(r)\mathbf{e}_r + \mathbf{e}_z \right), \qquad (3.2)$$

with a total curvature given by the sum of the slab (κ_s) and axisymmetric (κ_a) components, where

$$\kappa = \nabla \cdot \mathbf{n} = \kappa_s + \kappa_a, \quad \kappa_s = -\frac{z_s''(r)}{\left(1 + [z_s'(r)]^2\right)^{3/2}}, \quad \kappa_a = -\frac{z_s'(r)}{r\left(1 + [z_s'(r)]^2\right)^{1/2}}. \qquad (3.3)$$

Here $'$ denotes d/dr. With D_0 as the steady axial detonation phase speed, the shock angle ϕ between the axial direction and the surface normal $\mathbf{n}$ at any point on the surface is determined by

$$\cos\phi = \frac{D_n}{D_0} = \frac{1}{|\nabla S|} = \frac{1}{\left(1 + [z_s'(r)]^2\right)^{1/2}}, \quad \frac{dz_s}{dr} = -\tan\phi, \qquad (3.4)$$

so that κ can be written as

$$\kappa = \kappa_s + \kappa_a, \quad \kappa_s = \frac{d\phi}{d\xi}, \quad \kappa_a = \frac{\sin\phi}{r}, \qquad (3.5)$$

where ξ is the surface arc length. Switching to ϕ as the independent variable, the (r, z) components of the surface shape can then be calculated by integration of

$$\frac{dr}{d\phi} = \frac{\cos\phi}{\kappa_s}, \quad \frac{dz}{d\phi} = -\frac{\sin\phi}{\kappa_s}, \qquad (3.6)$$

subject to

$$z(\phi = 0) = 0, \; r(\phi = 0) = 0, \; \text{and } r(\phi = \phi_{edge}) = R, \qquad (3.7)$$

where ϕ_{edge} is the shock angle at the edge of the explosive ($r = R$). For all the experiments described in section 2, the explosive is unconfined, and the edge angle will correspond to

the sonic angle ($\phi_{edge} = \phi_s$) of the explosive (Bdzil & Stewart 2007). Due the $1/r$ term in the axisymmetric curvature component in (3.5), the integration of (3.6) is started at a finite small value of ϕ, where

$$r \sim \frac{\phi}{\kappa_s(\phi = 0)}, \quad z \sim -\frac{\phi^2}{2\kappa_s(\phi = 0)}, \quad \phi \ll 1, \tag{3.8}$$

and on $\phi = 0$,

$$D_n = D_0, \quad \kappa_s(\phi = 0) = \kappa_a(\phi = 0), \quad \kappa = 2\kappa_s(\phi = 0), \quad \text{where } \kappa_s(\phi = 0) = f(D_0)/2. \tag{3.9}$$

If both ϕ_{edge} and the phase speed D_0 are specified, the surface shape $z_s(r)$ and rate-stick radius R are determined by a single integration of (3.6) from $\phi = 0$ to $\phi = \phi_{edge}$. On the other hand, if both ϕ_{edge} and R are specified, the phase speed D_0 consistent with these specifications would be determined by a sequence of integrations of (3.6) and iteration on D_0 until $r = R$ at $\phi = \phi_{edge}$.

For the 2D slab geometry, the above analysis is repeated, except that $\kappa_a = 0$, while r now refers to the distance from the slab center to the slab edge. Boundary conditions (3.7) with $r(\phi = \phi_{edge}) = T/2$, where T is the slab thickness, can be applied directly to the integration of (3.6).

3.1.2. *The $R/T < 1$ scaling for lower-order DSD*

Here we show that any detonation whose propagation can be represented by the lower-order DSD form (3.1) with $d\kappa_s/dr > 0$, i.e. where the slab curvature component increases with increasing r, must have $R/T < 1$. Consider the rate-stick configuration. Note the slab component of curvature can be written as

$$\kappa_s = \cos\phi \frac{d\phi}{dr} = \frac{d(\sin\phi)}{dr}, \tag{3.10}$$

where $\kappa_s > 0$. From (3.3), the total curvature κ is then

$$\kappa = \frac{d(\sin\phi)}{dr} + \frac{\sin\phi}{r}. \tag{3.11}$$

We now additionally assume that

$$\frac{d\kappa_s}{dr} = \frac{d^2(\sin\phi)}{d^2 r} > 0 \text{ for } r > 0, \tag{3.12}$$

where $d\kappa_s/dr = 0$ on $r = 0$ from (3.8). Application of the mean value theorem to the function (3.11) with the constraint (3.12) implies that

$$\frac{d(\sin\phi)}{dr} > \frac{\sin\phi}{r} \text{ for } r > 0, \tag{3.13}$$

i.e. at each radial component r, the slab component of curvature is greater than the corresponding axisymmetric component. The two components are equal on $r = 0$. Now, for a given phase velocity D_0, the rate-stick radius R at which $\phi = \phi_{edge}$ is determined from the integration of

$$\frac{d(\sin\phi)}{dr} + \frac{\sin\phi}{r}\bigg|_{rs} = f(D_0 \cos\phi), \tag{3.14}$$

where $|_{rs}$ denotes the rate-stick geometry. Similarly, in the slab geometry, the slab height $T/2$ at which $\phi = \phi_{edge}$ for the same phase velocity D_0 is determined from the integration

of

$$\left.\frac{d(\sin\phi)}{dr}\right|_{slab} = f(D_0 \cos\phi), \tag{3.15}$$

where $|_{slab}$ denotes the slab geometry. However, by applying the inequality (3.13) to (3.14), it can also be shown that

$$2\left.\frac{d(\sin\phi)}{dr}\right|_{rs} = \left.\frac{d(\sin\phi)}{d(r/2)}\right|_{rs} > f(D_0 \cos\phi). \tag{3.16}$$

By comparing (3.15) and (3.16), it follows that for each phase velocity D_0, R and T must satisfy the inequality

$$R/2 < T/2 \text{ or } R/T < 1. \tag{3.17}$$

The implication of (3.17) for the size effect curves is that when D_0 is plotted with $1/R$ for the rate-stick, and with $1/T$ for the slab, the slab thickness-effect curve must lie to the left of the rate-stick diameter-effect curve. In section 2, this was shown to be the case for the experimentally determined size-effect curves for PBX 9501, PBX 9502 and ANFO.

3.1.3. D_n-κ forms for PBX 9501, PBX 9502 and ANFO

We now examine the previously calibrated lower-order DSD (or $D_n - \kappa$) fits for PBX 9501, PBX 9502 and ANFO. These have the functional form,

$$\frac{D_n}{D_{CJ}} = 1 + A\left((C_1 - \kappa)^{e_1} - C_1^{e_1}\right) - B\kappa\left(\frac{1 + C_2\kappa + C_3\kappa^2}{1 + C_4\kappa + C_5\kappa^2}\right), \tag{3.18}$$

where A, B, C_1, C_2, C_3, C_4, C_5 and e_1 (if $A \neq 0$) are fitting parameters. In some cases the Chapman-Jouguet velocity D_{CJ} and the sonic angle ϕ_s are also used as fitting parameters, or alternatively prescribed fixed values that are associated with the state properties of the explosive. Parameter values for the $D_n - \kappa$ relation (3.18) for each explosive are listed in table 9, where each calibration is based solely on experimental data obtained in the rate-stick configuration.

For PBX 9501, the calibration is from Aslam (2007), based on the twelve rate-stick diameter-effect points along with the two shock shape records reported in table 3. The calibration for PBX 9502 is specific to lot 008 and was calculated by Bdzil (2003) using the rate-stick diameter-effect points and associated shock shape data from shots 15-2839, 15-2529 and 15-2851 in table 6. The calibration for ANFO was again by Bdzil (2008). The calibration was based on the 14 rate-stick diameter-effect points shown in table 8 along with the 10 shock shapes that were available from the tests (these tests have the recorded shot numbers in table 8). It represents a fit of the non-overlapping $D_n - \kappa$ data reported in Bdzil *et al.* (2002).

For PBX 9502, we explore a second $D_n - \kappa$ relation due to Hill & Aslam (2010) that accounts for the effect of an initial density variation relative to a nominal density. The $D_n - \kappa$ relation is of the form

$$\frac{D_n}{D_{CJ}} = 1 - B_1\kappa\left(\frac{1 + c_2B_1\kappa + c_3(B_1\kappa)^2}{1 + c_4B_1\kappa + c_5(B_1\kappa)^2}\right), \tag{3.19}$$

where

$$D_{CJ} = D_{CJ_n}\left(1 + c_6\left(\frac{\rho_0}{\rho_{0_n}} - 1\right)\right) \quad \text{and} \quad \frac{B_1}{B_{l008}} = 1 + c_7\left(\frac{\rho_0}{\rho_{0_n}} - 1\right). \tag{3.20}$$

Here D_{CJ_n} is the Chapman-Jouguet speed at the nominal density ρ_{0_n}. The calibration

	PBX 9501	PBX 9502	ANFO
D_{CJ} (cm/μs)	0.8795	0.775525188	0.48
A (cm^{e_1})	1.175	0	0
B (cm)	0.003655	0.232582927	2.350
C_1 (cm^{-1})	24.43	-	-
C_2 (cm)	0.005693	0.458557510	0.07563
C_3 (cm^2)	0	$2.11968814 \cdot 10^{-6}$	28.93
C_4 (cm)	0.4313	5.97541313	3.933
C_5 (cm^2)	0	$1.45459626 \cdot 10^{-8}$	0.02649
e_1	0.07780	-	-
ϕ_s	0.62999632	0.7033841	0.44

TABLE 9. Fits to the DSD propagation law given by (3.18) for PBX 9501, PBX 9502 (lot 008) and ANFO. Units as originally published.

D_{CJ_n} (cm/μs)	0.78
ρ_{0_n} (g/cm^3)	1.890
B_{l008} (cm)	0.44923
c_2	4.8707
c_3	2.7768
c_4	32.115
c_5	78.183
c_6	1.5885
c_7	61.133
ϕ_s	0.61089633

TABLE 10. Parameter fit to the density-corrected DSD propagation law given by (3.19) and (3.20) for PBX 9502 (lot 008). Units as originally published.

in Hill & Aslam (2010), which also involved the effect of initial temperature variations relative to room temperature, was done using 50 rate-stick diameter-effect points and 22 shock shapes obtained from experiments across a range of PBX 9502 lots and initial density and temperature conditions. The available density range used in the calibration was 1.890±0.005 g/cc. The PBX 9502 calibration parameters for (3.19) and (3.20) specific to lot 008 at room temperature is given in table 10.

3.2. *Higher-order DSD*

It has been recognized previously that for certain explosives, especially those that are classified as non-ideal, the experimentally observed normal detonation velocity variation with curvature cannot be captured with the leading-order DSD theory (Kennedy 1998; Bdzil *et al.* 2002). Consequently, attempts have been made to incorporate additional physics, in particular those resulting from detonation front acceleration and from transverse flow. Brun (see Brun *et al.* (1994)) incorporated the acceleration term DD_n/Dt in an *ad hoc* fashion, proposing the higher-order intrinsic evolution equation

$$\frac{DD_n}{Dt} = -C(D_n)(\kappa - K(D_n)), \tag{3.21}$$

where C and K are functions of D_n. Yao & Stewart (1996) and Kasimov & Stewart (2005) sought to incorporate the acceleration term DD_n/Dt in a more systematic fashion by examining the relative magnitudes of the DD_n/Dt, $D_{CJ} - D_n$ and κ terms, and

subsequently incorporating the DD_n/Dt and κ contributions at the same order. Contributions arising from transverse flow terms were neglected. Consequently, the derived high-order evolution equations have hyperbolic wave-like characteristic properties. Aslam & Stewart (1999) calibrated a hyperbolic higher-order evolution equation of the form

$$\frac{DD_n}{Dt} = -\frac{D_n^2 \kappa}{2} + \beta(D_n), \tag{3.22}$$

to properties of a reactive Euler model, and showed that solutions to the evolution equation provided a good approximation to a direct numerical simulation of the Euler equations in geometries with perfectly confining walls. For problems where the shape of the wave is specified at the HE/material boundary due to confinement effects, the direction of the characteristics in these hyperbolic higher-order equations may limit the range of edge angles that can be considered (Bdzil *et al.* 2002). To the authors' knowledge, there have not been any attempts to parameterize the hyperbolic higher-order DSD evolution equations, which include only the addition of the front acceleration terms, to the rate-stick diameter effect or slab thickness effect and shock shapes for PBX 9501, PBX 9502 or ANFO, and thus we will not consider the hyperbolic forms further in this study.

For insensitive and non-ideal high explosives, a higher-order intrinsic surface evolution equation for DSD has been developed which accounts for the two effects of front acceleration and transverse flow (Aslam *et al.* 1998; Bdzil *et al.* 2002). Due to the inclusion of transverse flow, the resulting higher-order evolution equation has a parabolic structure. In the axisymmetric rate stick configuration, this evolution equation takes the form,

$$\kappa = \kappa_s + \frac{\sin\phi}{r} = F(\mathcal{D}) - M(\mathcal{D})\frac{D\mathcal{D}}{Dt} + N(\mathcal{D})\frac{\partial^2 \mathcal{D}}{\partial \xi^2}, \quad \mathcal{D} = \frac{D_n}{D_{CJ}} - 1, \tag{3.23}$$

while for the slab geometry the axisymmetric curvature component $(\sin\phi)/r$ is omitted. Here, $M(\mathcal{D}) \geqslant 0$, $N(\mathcal{D}) \geqslant 0$ and $F(\mathcal{D}) > 0$. The front acceleration $(M \cdot D\mathcal{D}/Dt)$ and transverse flow $(N \cdot \partial^2 \mathcal{D}/\partial \xi^2)$ components arise as the first correction terms to the leading-order $\kappa = F(\mathcal{D})$ evolution equation in a systematic asymptotic analysis of the front propagation dynamics based on the standard DSD scalings of slow time evolution and small curvature (Aslam *et al.* 1998).

3.2.1. *Higher-order DSD: Steady Propagation in Rate-Stick and Slab Geometries*

We now consider steady solutions of the parabolic higher-order DSD evolution equation given by (3.23), where in a rate-stick or slab configuration,

$$D_n = D_0 \cos(\phi), \quad \frac{D\mathcal{D}}{Dt} = -D_{CJ}\left(\frac{D_0}{D_{CJ}}\sin(\phi)\right)^2 \kappa_s,$$
$$\frac{\partial^2 \mathcal{D}}{\partial \xi^2} = -\frac{D_0}{D_{CJ}}\left(\sin(\phi)\frac{d\kappa_s}{d\xi} + \cos(\phi)\kappa_s^2\right). \tag{3.24}$$

For a rate-stick, the steady form of (3.23) becomes

$$\kappa_s \frac{D_0}{D_{CJ}}\sin(\phi)\frac{d\kappa_s}{d\phi} =$$
$$-\frac{D_0}{D_{CJ}}\cos(\phi)\kappa_s^2 - \frac{1}{N}\left(\kappa_s + \frac{\sin(\phi)}{r} - F - D_{CJ}\left(\frac{D_0}{D_{CJ}}\sin(\phi)\right)^2 M\kappa_s\right). \tag{3.25}$$

D_{CJ} (mm/μs)	5.2
N (mm)	28.4
M (μs·mm^{-1})	$(5.87+1.41\times10^{-1}N$(mm)$)/D_{CJ}$ (mm/μs)
F_1	$1.34\times10^{-2}+8.6\times10^{-5}N$(mm)
F_2 (mm^{-1})	$3.52\times10^{-2}+7.6\times10^{-5}N$(mm)
ϕ_s	0.5

TABLE 11. Parameter fit to the higher-order DSD propagation law given by (3.23) and (3.28) for ANFO

Given ϕ_{edge} and R, the phase velocity D_0 is obtained by solving (3.25) together with (3.6) subject to boundary conditions (3.7). Again, integration must begin at a small finite value of ϕ using (3.8), where on $\phi = 0$,

$$\kappa_s = \frac{D_{CJ}}{D_0 N}\left(-1 + \left[1 + \frac{D_0}{D_{CJ}}NF_c\right]^{\frac{1}{2}}\right), \quad F_c = F\left(\frac{D_0}{D_{CJ}} - 1\right). \qquad (3.26)$$

Similarly, for a slab, the phase velocity D_0 is obtained by solving (3.25), omitting the $\sin(\phi)/r$ term, with (3.6) subject to (3.7). However, as for the rate stick, integration must also begin at a small finite value of ϕ using (3.8), where on $\phi = 0$,

$$\kappa_s = \frac{D_{CJ}}{2D_0 N}\left(-1 + \left[1 + 4\frac{D_0}{D_{CJ}}NF_c\right]^{\frac{1}{2}}\right), \quad F_c = F\left(\frac{D_0}{D_{CJ}} - 1\right). \qquad (3.27)$$

3.2.2. $DD_n/Dt - D_{n,\xi\xi} - D_n - \kappa$ form for ANFO

A calibration of the higher-order DSD equation (3.23) for ANFO has been provided by Bdzil *et al.* (2002) assuming the functional forms

$$F(\mathcal{D}) = -F_1\mathcal{D}\exp\left(-F_2/(\mathcal{D}+1)\right), \quad M(\mathcal{D}) = \text{constant}, \quad N(\mathcal{D}) = \text{constant}. \qquad (3.28)$$

Parameter values are shown in table 11. The parameter calibration was again based on the 14 rate-stick diameter-effect points shown in table 8 along with the 10 shock shapes that were available from the tests. (Note that the expression for M in table 11 is divided by a factor of D_{CJ} from that reported in Bdzil *et al.* (2002), since the D_{CJ} term correctly multiplying the steady front acceleration term in (3.25) was omitted in the analysis by Bdzil *et al.* (2002). Consequently, the leading-order transverse signaling speed, which is proportional to the inverse of the square root of M, should be greater than that observed in Bdzil *et al.* (2002). This correction results in a faster relaxation time to steady state propagation for the unsteady higher-order DSD evolution equation (3.23) for ANFO, potentially addressing a point of concern regarding the use of higher-order DSD theories raised in Bdzil *et al.* (2002)).

3.3. *Comparison of DSD Predictions with Slab and Rate-Stick Experimental Results*

Figure 9 shows the lower-order DSD-calculated PBX 9501 diameter- and thickness-effect curves using the $D_n - \kappa$ relation (3.18) with table 9 parameters for unconfined, $\phi = \phi_s$, rate-stick (D_0 vs. $1/R$) and slab (D_0 vs. $1/T$) geometries. Also plotted are the corresponding experimentally calculated points from tables 2 and 3. Given that the PBX 9501 $D_n - \kappa$ relation was calibrated using the rate-stick data only, unsurprisingly we observe a good fit between the DSD diameter-effect curve and the rate-stick data. Using the $D_n - \kappa$ relation (3.18) with table 9 parameters, the DSD thickness-effect curve for the slab geometry captures the experimental data reasonably well for thicker slabs, but
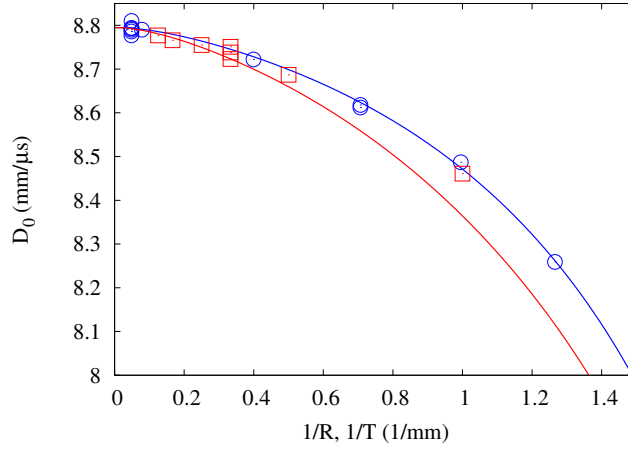
FIGURE 9. Diameter-effect variation for PBX 9501 rate-sticks (D_0 vs. $1/R$, ○) and thickness-effect variation for PBX 9501 slabs (D_0 vs. $1/T$, □) with the corresponding rate-stick (blue line) and slab (red line) lower-order DSD predictions.
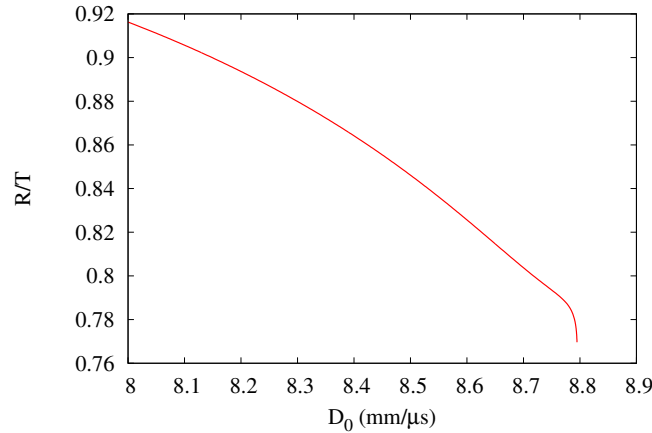

FIGURE 10. Variation of the PBX 9501 detonation phase velocity D_0 with the ratio of rate-stick radius R to slab thickness T that correspond to D_0 when $\phi = \phi_s$ at the rate-stick or slab edge.

deviates from the experimental data for thinner slabs, particularly for thicknesses of 1 and 2 mm. For the PBX 9501 $D_n - \kappa$ curve (3.18), the R/T scaling as a function of phase velocity D_0 is shown in figure 10. For D_0 close to D_{CJ}, there is a rapid increase in R/T, whereafter the scale factor R/T increases more slowly as D_0 decreases, reaching a value of $R/T = 0.916$ when $D_0 = 8$ mm/μs.

The components κ_s and κ_a as a function of radius in the DSD rate-stick calculation for $D_0 = 8.4$ mm/μs are shown in figure 11. Near the origin, the components are close in magnitude, but for increasing radius the slab component increasingly grows in magnitude relative to the axisymmetric component. From figure 9, the slab thickness-effect curve when plotted as D_0 vs. $1/T$ lies to the left of the rate-stick diameter-effect curve when plotted as D_0 vs. $1/R$, and with $\kappa_s > \kappa_a$ across the rate stick, reinforces the discussion in section 3.1.2 on the consequence of differing components of curvature. The disparity in the curvature components across the rate-stick for the lower-order DSD model may
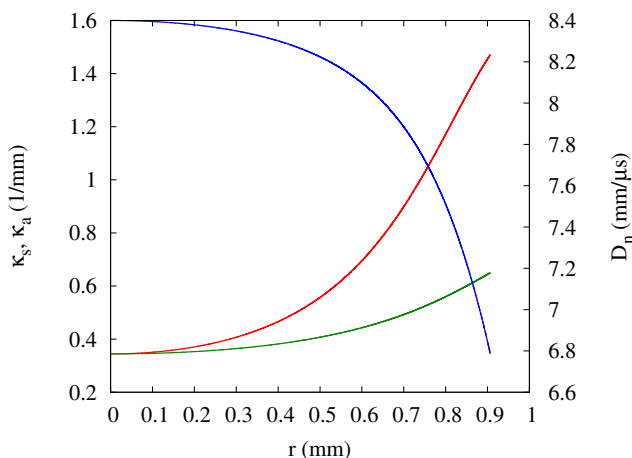
FIGURE 11. Slab κ_s (red) and axisymmetric κ_a (green) components of curvature along with D_n (blue) in a PBX 9501 rate-stick from $r = 0$ to $r = R$ calculated when $D_0 = 8.4$ mm/μs.

indicate a higher-order DSD model is required to fit the smaller diameter rate-sticks. Also shown in figure 11 is the magnitude of the normal velocity component D_n across the rate-stick. A significant decrease in D_n relative to the phase velocity D_0 occurs with increasing radius. The curvature components κ_s and κ_a and the normal detonation velocity D_n as a function of radius for the PBX 9501 DSD rate-stick calculation for $D_0 = 8.7948$ mm/μs are shown in figure 12. This is in a regime where $D_0 \sim D_{CJ}$, explored asymptotically in section 4. For most of the rate-stick, the curvature components are small, but $\kappa_s > \kappa_a$ everywhere except at $r = 0$ where $\kappa_s = \kappa_a$. The magnitude of the slab component κ_s rises rapidly in a boundary layer at the edge of the rate-stick to meet the requirement $\phi = \phi_s$.

Figure 13 shows the DSD calculated PBX 9502 size-effect curves using the $D_n - \kappa$ relation (3.18) with table 9 parameters for unconfined, $\phi = \phi_s$, rate-stick (D_0 vs. $1/R$) and slab (D_0 vs. $1/T$) geometries. Also plotted are the corresponding experimentally calculated points from tables 5 and 6, the slab experimental points corrected to a density of 1.886 g/cc using the method described in section 2, and the PBX 9502 thickness-effect curve for slabs using the density dependent PBX 9502 $D_n - \kappa$ relation (3.19) and (3.20) for parameters in table 10 with $\rho_0 = 1.874$ g/cc. Again, given that the PBX 9502 $D_n - \kappa$ calibration was obtained via use of the rate-stick data, we observe a good fit between the DSD diameter-effect curve and the rate-stick data. The slab thickness-effect curve generated using the $D_n - \kappa$ relation (3.18) with table 9 parameters agrees reasonably well with the slab experimental data, even though the experimental data was generated using lower density HE than used for the rate-sticks. When this slab data is corrected to a density of 1.886 g/cc using the extrapolation procedure described in section 2, the agreement between the slab data and the DSD thickness-effect curve from the D_n-κ relation (3.18) is good. The $D_n - \kappa$ relations (3.19) and (3.20) can also be used to generate a slab thickness-effect curve with $\rho_0 = 1.874$ g/cc, a value close to the density of the slabs used in the testing (table 5). Despite being used outside of its fitting regime ($\rho_0 = 1.890 \pm 0.005$ g/cc), the DSD generated thickness-effect curve approximates the 8, 12 and 16 mm thick slabs well, but thereafter generates a phase velocity significantly above the experimental data.

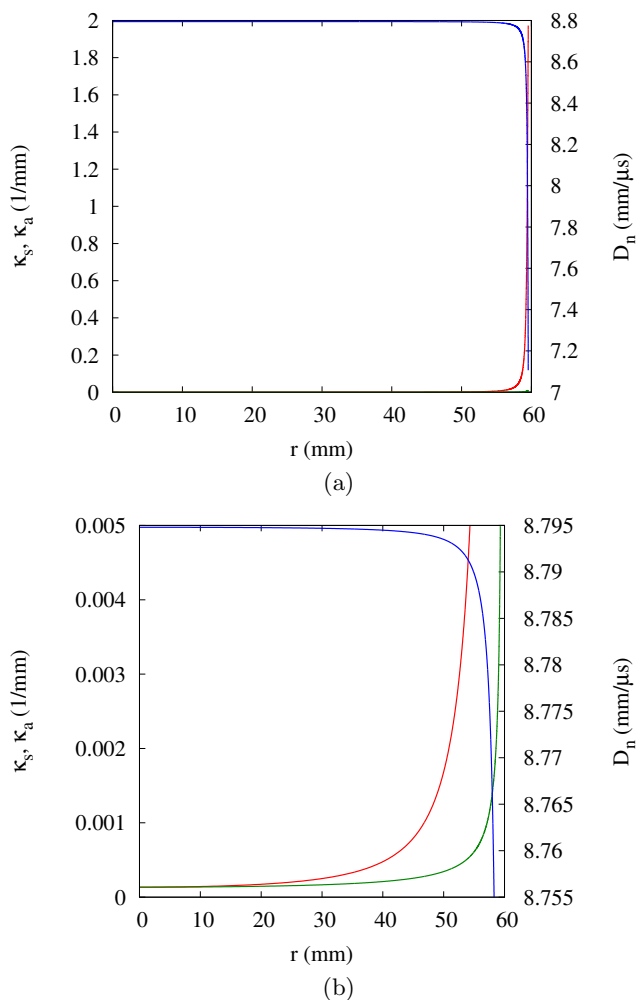Figure 13 also shows the regions of $1/R$ (rate-stick) and $1/T$ (slab) in which detonation

FIGURE 12. Slab κ_s (red) and axisymmetric κ_a (green) components of curvature along with D_n (blue) in a PBX 9501 rate-stick from $r = 0$ to $r = R$ calculated when $D_0 = 8.7948$ mm/μs. (a) Full range of κ_s, κ_a and D_n shown. (b) Magnified region for $(\kappa_s, \kappa_a) < 0.005$.

failure is observed to occur experimentally. As described in section 2, for PBX 9502 rate-sticks, the failure region is located between the radii 4 mm and 3.75 mm, while for slabs the failure region is located between slabs of 3.75 mm and 3.5 mm thickness. Thus at failure, $R_c/T_c > 1$, whereas for the velocity effect curves, $R/T < 1$. As noted above, since DSD is based on a quasi-steady flow assumption, while detonation failure involves an inherently unsteady process, the DSD construction is not suitable for describing failure limits. However, an extrapolation of each of the diameter- and thickness-effect curves shown in figure 13 into their corresponding regions of failure implies a crossing would occur and the ratio R/T at failure in each geometry would become greater than one.

For the PBX 9502 $D_n - \kappa$ relation (3.18), the R/T scaling as a function of phase velocity D_0 is shown in figure 14 for no confinement $(\phi = \phi_s)$ at the explosive edge. For D_0 close to D_{CJ}, there is a rapid increase in R/T. The ratio R/T subsequently increases at a slower rate and then decreases. The region in which R/T begins to decrease corresponds approximately to a regime where there is a change in slope in the diameter- and
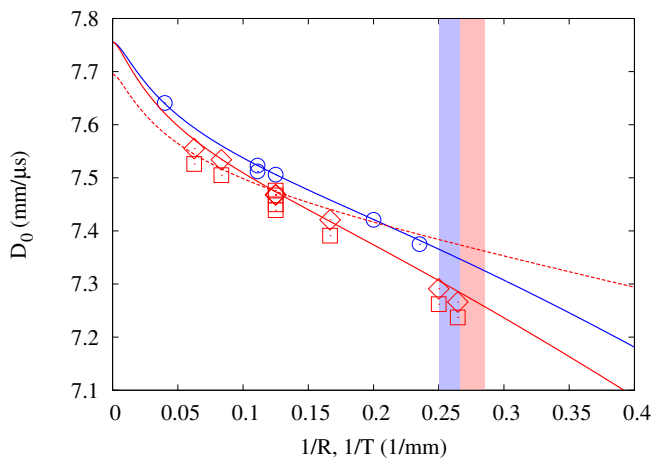
FIGURE 13. Diameter- and thickness-effect variation for PBX 9502 rate-sticks (D_0 vs. $1/R$, ○) and PBX 9502 slabs (D_0 vs. $1/T$, □) with the corresponding rate-stick (solid blue line) and slab (solid red line) DSD predictions based on (3.18). Also, shown are the slab data points (◇) modified to a starting density of 1.886 g/cc and the slab thickness-effect DSD prediction from (3.19) and (3.20) with $\rho_0 = 1.874$ g/cc (dashed red line). The light blue ■ and red ■ blocks indicate the region of $1/R$ (3.75 mm < R < 4 mm) and $1/T$ (3.5 mm < T < 3.75 mm) in which detonation failure occurs in the rate-stick and slab geometries respectively.
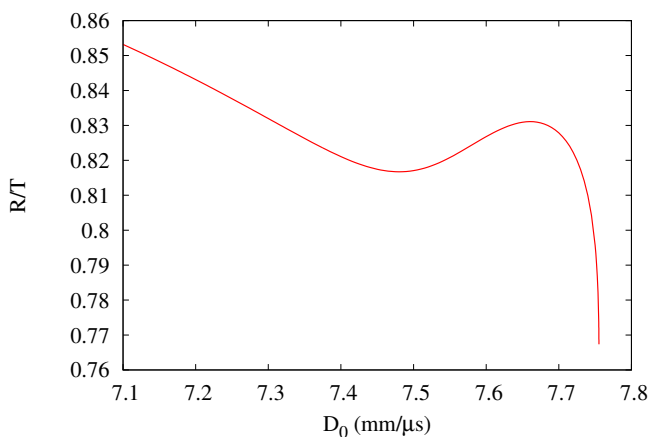
FIGURE 14. Variation of the PBX 9502 detonation phase velocity D_0 with the ratio of rate-stick radius R to slab thickness T that correspond to D_0 when $\phi = \phi_s$ at the rate-stick or slab edge.

thickness-effect curves (figure 13). The change in slope occurs when the sonic plane in the non-planar PBX 9502 detonation has transitioned through the slow carbon coagulation reaction layer, and subsequently resides close to the end of the fast heat release layer (Bdzil *et al.* 2006). Thereafter the scale factor R/T increases as D_0 decreases, reaching a value of $R/T = 0.853$ when $D_0 = 7.1$ mm/μs. Figure 15 shows the curvature components κ_s and κ_a and the normal detonation velocity D_n as a function of radius in the DSD rate-stick calculation for $D_0 = 7.5$ mm/μs and $\phi = \phi_s$ at $r = R$. Over half of the radius $\kappa_a \approx \kappa_s$, but subsequently the slab component increasingly grows in magnitude relative to the axisymmetric component. Again, the slab thickness-effect curve when plotted as D_0 vs. $1/T$ lies to the left of the rate-stick diameter-effect curve when plotted as D_0
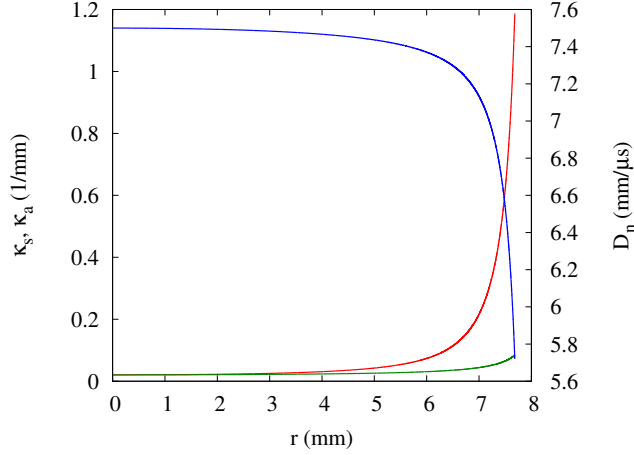
FIGURE 15. Slab κ_s (red) and axisymmetric κ_a (green) components of curvature along with D_n (blue) in a PBX 9502 rate-stick from $r = 0$ to $r = R$ calculated when $D_0 = 7.5$ mm/μs and $\phi = \phi_s$ at $r = R$.

vs. $1/R$ (section 3.1.2). The normal detonation velocity shows an order one decrease in magnitude across the rate-stick.

The curvature components κ_s and κ_a as a function of radius in the PBX 9502 DSD rate-stick calculation for $D_0 = 7.75524$ mm/μs and $\phi = \phi_s$ ar $r = R$ are shown in figure 16. This is in a regime where $D_0 \sim D_{CJ}$, and for most of the rate-stick, the curvature components are small, but $\kappa_s > \kappa_a$ everywhere. As is the case for PBX 9501, the magnitude of the slab component κ_s rises rapidly in a boundary layer at the edge of the rate-stick to meet the requirement $\phi = \phi_s$.

Figure 17 shows the lower-order DSD-calculated ANFO size-effect curves using the $D_n - \kappa$ relation (3.18) with table 9 parameters for unconfined, $\phi = \phi_s$, rate-stick (D_0 vs. $1/R$) and slab (D_0 vs. $1/T$) geometries. The ANFO $D_n - \kappa$ calibration was obtained via use of the rate-stick data, and consequently a good fit between the DSD diameter-effect curve and the rate-stick data is observed. However, when plotted as D_0 vs. $1/T$, the lower-order DSD predicted thickness-effect curve for the slab lies close to the diameter-effect curve for the rate-stick, but is a poor fit to the experimental thickness-effect data points for the slab. Also shown are the ANFO diameter and thickness-effect curves based on the higher-order DSD theory (3.23) and (3.28) with table 11 parameters. The thickness-effect curve for the slab geometry generated by the higher-order DSD theory (calibrated to the rate-stick diameter-effect data) provides a significantly better representation of the slab data than that with the lower-order $D_n - \kappa$ theory. This includes the presence of an inflection point in the thickness-effect curve that also appears to be a property of the slab data. The deviation of the higher-order DSD size-effect curves from the data at larger HE dimensions is due to the value of $D_{CJ} = 5.2$ km/s used in the calibration of the higher-order DSD relation (Bdzil *et al.* 2002). This was obtained from an extrapolation based on the "dice throw" series of large scale ANFO tests (Helm *et al.* 1976). Subsequent analysis by Bdzil (2008) of the more carefully controlled ANFO rate-stick test series (Bdzil *et al.* 2002) led to the recommendation to lower D_{CJ} to 4.8 km/s, as used by Bdzil (2008) in the calibration of the lower-order $D_n - \kappa$ form of the DSD relation for ANFO (table 9). This suggests that a recalibration of the higher-order DSD theory for ANFO based on a lower value of D_{CJ} would result in an even closer agreement between the size-effect predictions of the higher-order DSD theory and the experimental data.
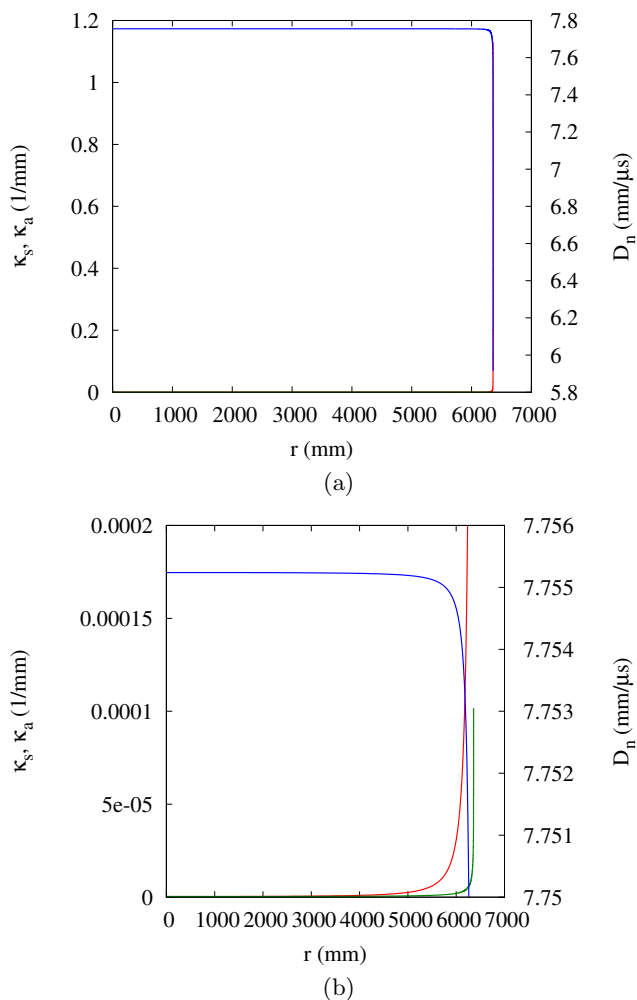
FIGURE 16. Slab κ_s (red) and axisymmetric κ_a (green) components of curvature along with D_n (blue) in a PBX 9502 rate-stick from $r = 0$ to $r = R$ calculated when $D_0 = 7.75524$ mm/μs and $\phi = \phi_s$ at $r = R$. (a) Full range of κ_s, κ_a and D_n shown. (b) Magnified region for $(\kappa_s, \kappa_a) < 0.0002$.

The relative closeness of the lower-order $D_n - \kappa$ theory based size-effect curves for the slab and rate-stick geometries, when plotted as D_0 vs. $1/T$ and D_0 vs. $1/R$ respectively, points to a R/T scaling of unity. This is reflected in figure 18, where D_0 is plotted as a function of the scale factor R/T using the lower-order $D_n - \kappa$ DSD relation. There is a rapid increase in R/T as D_0 decreases slightly from D_{CJ}. The scale factor reaches a value of 0.951 when $D_0 = 4$ mm/μs and 0.996 when $D_0 = 1.5$ mm/μs. Relative to the observed R/T scale factor in the experimental size-effect data, the $D_n - \kappa$ calibration via (3.18) and table 9 is assigning too much weight to the axisymmetric curvature component κ_a. This is confirmed in figure 19, where the components κ_s and κ_a as a function of radius in the DSD rate-stick calculation for $D_0 = 2.5$ mm/μs are shown. It is clear that $\kappa_s \approx \kappa_a$. Based on the discussion in section 3.1.2, in order to match the ANFO slab thickness-effect data, the slab curvature component across the rate-stick should be significantly greater than the axisymmetric component. Also shown in figure 18 is the scale factor R/T calculated
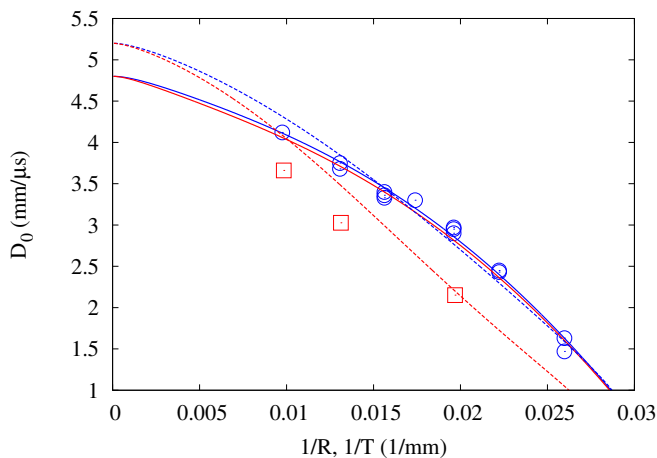
FIGURE 17. Diameter- and thickness-effect variation for ANFO rate-sticks (D_0 vs. $1/R$, $\circ$) and ANFO slabs (D_0 vs. $1/T$, $\square$) with the corresponding rate-stick (solid blue line) and slab (solid red line) DSD predictions based on (3.18) and table 9. Also shown are the rate-stick (blue dashed line) and slab (red dashed line) ANFO size-effect predictions based on the higher-order DSD theory (3.23) and (3.28) with table 11 parameters.
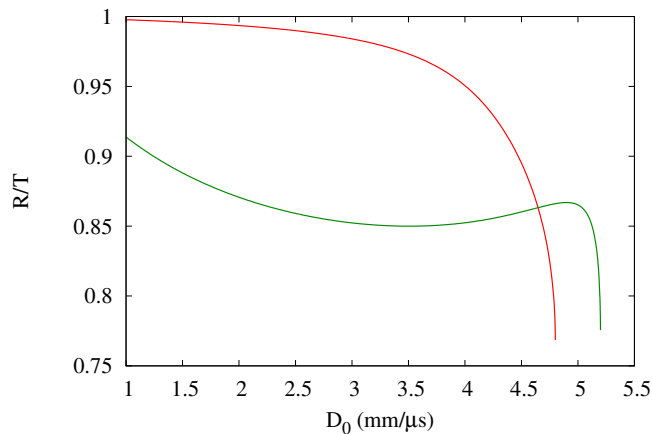

FIGURE 18. Variation of the ANFO detonation phase velocity D_0 with the ratio of rate-stick radius (R) to slab thickness (T) that correspond to D_0 when $\phi = \phi_s$ at the rate-stick or slab edge. The red line is based on the lower-order $D_n - \kappa$ form (3.18), while the green line is from the higher-order DSD theory (3.25) and (3.28).

from the higher-order DSD theory. Again there is a rapid increase in R/T as D_0 decreases slightly from D_{CJ} (5.2 mm/μs in this case). Subsequently, D_0 drops significantly for a moderate change in the scale factor. For the higher-order DSD based theory, the slab component of curvature is now significantly larger than the axisymmetric component across the rate-stick (figure 20).

The curvature components κ_s and κ_a as a function of radius for the ANFO lower-order $D_n - \kappa$ based DSD rate-stick calculation for $D_0 = 4.799$ mm/μs are shown in figure 21. As seen previously for PBX 9501 and PBX 9502, the magnitude of the slab component
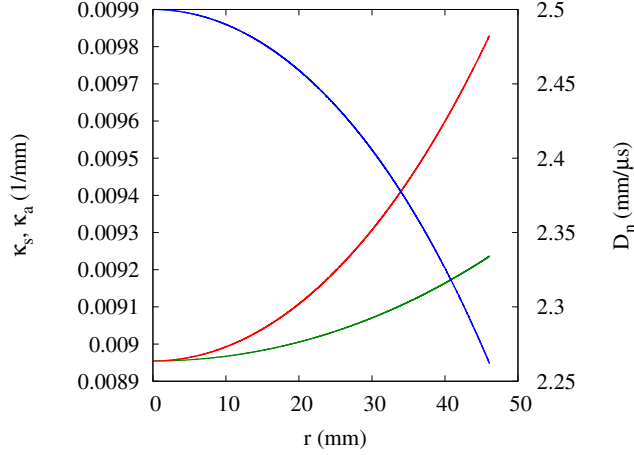
FIGURE 19. Slab κ_s (red) and axisymmetric κ_a (green) components of curvature along with D_n (blue) in an ANFO rate-stick from $r = 0$ to $r = R$ calculated when $D_0 = 2.5$ mm/μs for the lower-order $D_n - \kappa$ based DSD theory.

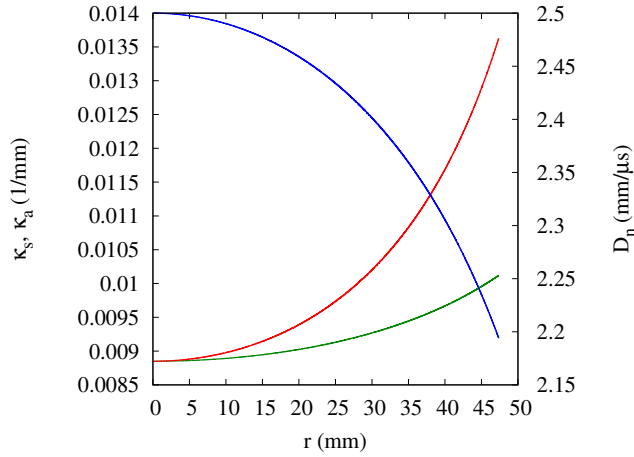FIGURE 20. Slab κ_s (red) and axisymmetric κ_a (green) components of curvature along with D_n (blue) in an ANFO rate-stick from $r = 0$ to $r = R$ calculated when $D_0 = 2.5$ mm/μs for the higher-order DSD theory.

κ_s rises rapidly in a boundary layer at the edge of the rate-stick to meet the requirement $\phi = \phi_s$.

4. Scaling Behaviour for $D_0 \to D_{CJ}$

Here we conduct an asymptotic analysis of the lower-order DSD model in the limit where the detonation phase velocity D_0 approaches D_{CJ}. The analysis gives a detailed insight into both the dynamics behind the variation in the propagation scale factor R/T and the multi-layer behavior of the DSD surface shapes for different degrees of confinement. Rather than the more complex forms studied in section 3, here we assume a $D_n - \kappa$
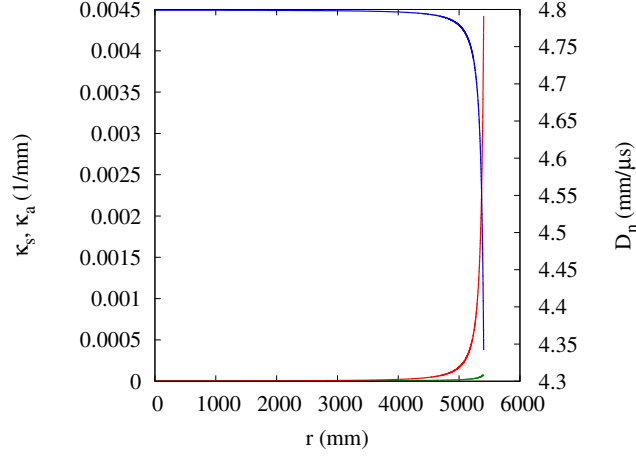
FIGURE 21. Slab κ_s (red) and axisymmetric κ_a (green) components of curvature along with D_n (blue) in an ANFO rate-stick from $r = 0$ to $r = R$ calculated when $D_0 = 4.799$ mm/μs for the $D_n - \kappa$ based theory.

law of the linear form

$$\frac{D_n}{D_{CJ}} = 1 - B\kappa, \tag{4.1}$$

which allows the solutions in individual layers to be derived analytically. Note that the parameter B represents a length scale that is characteristic of the reaction zone thickness. We are interested in the limit $D_0 \to D_{CJ}$, and define a small parameter ϵ such that

$$\epsilon = 1 - \frac{D_0}{D_{CJ}}, \quad \epsilon \ll 1. \tag{4.2}$$

Consequently, with (4.1) and (3.4), the scaled curvatures $B\kappa_s$ and $B\kappa_a$ become

$$B\kappa_s = 1 - (1 - \epsilon)\cos\phi, \quad B\kappa_s + \frac{\sin\phi}{(r/B)} = 1 - (1 - \epsilon)\cos\phi, \tag{4.3}$$

in the slab and rate-stick geometries respectively.

4.1. *Slab Geometry*

For the slab geometry, differential equations (3.6) for $r(\phi)$ and $z(\phi)$ become

$$[1 - (1 - \epsilon)\cos\phi]\frac{d(r/B)}{d\phi} = \cos\phi, \quad [1 - (1 - \epsilon)\cos\phi]\frac{d(z/B)}{d\phi} = -\sin\phi, \tag{4.4}$$

subject to boundary conditions (3.7). Although these equations can be integrated exactly (Bdzil 1981), we are interested in the structure of the solutions for $\epsilon \ll 1$. We find an inner layer in the central part of the charge described by the scalings $\phi = \mathcal{O}(\sqrt{\epsilon})$, $r/B = \mathcal{O}(1/\sqrt{\epsilon})$ and $z/B = \mathcal{O}(1)$, where

$$\frac{r}{B} = \sqrt{\frac{2}{\epsilon}}\tan^{-1}\left(\frac{\phi}{\sqrt{2\epsilon}}\right) + \mathcal{O}(\sqrt{\epsilon}), \quad \frac{z}{B} = \ln 2 - \ln\left[2 + \frac{\phi^2}{\epsilon}\right] + \mathcal{O}(\epsilon). \tag{4.5}$$

In this layer the scaled curvature $B\kappa_s = \mathcal{O}(\epsilon)$, while deviations of D_n from D_{CJ} are $\mathcal{O}(\epsilon)$. Specifically, in terms of ϕ,

$$B\kappa_s = \epsilon\left(1 + \frac{\phi^2}{2\epsilon}\right) + \mathcal{O}(\epsilon^2), \quad D_n = D_{CJ}\left[1 - \epsilon\left(1 + \frac{\phi^2}{2\epsilon}\right)\right] + \mathcal{O}(\epsilon^2). \tag{4.6}$$

If the degree of confinement is such that $\phi_{edge} = \mathcal{O}(\sqrt{\epsilon})$, (4.5) describes the solution from the charge center to the charge edge. Note that contained within the inner layer is a region of size $\phi = \mathcal{O}(\epsilon)$ around $r = 0$ where $r/B = \mathcal{O}(1)$ and $z/B = \mathcal{O}(\epsilon)$, in which

$$\frac{r}{B} \sim \frac{\phi}{\epsilon}, \quad \frac{z}{B} \sim -\frac{\phi^2}{2\epsilon}, \quad B\kappa_s \sim \epsilon, \quad D_n = D_{CJ}(1 - \epsilon). \tag{4.7}$$

For $\phi_{edge} = \mathcal{O}(1)$, an outer layer must be appended to the inner layer which extends to the edge of the charge. In this layer, $\phi = \mathcal{O}(1)$, $r/B = \mathcal{O}(1/\sqrt{\epsilon})$ and $z/B = \mathcal{O}(\ln(1/\epsilon))$, where

$$\frac{r}{B} = \frac{\pi}{\sqrt{2\epsilon}} - \phi - \frac{1}{\tan(\phi/2)} + \mathcal{O}(\sqrt{\epsilon}), \quad \frac{z}{B} = -\ln(1/\epsilon) - \ln(1 - \cos\phi) + \mathcal{O}(\epsilon\ln(1/\epsilon)), \tag{4.8}$$

after matching with (4.5). Correspondingly, the scaled curvature $B\kappa_s = \mathcal{O}(1)$, while deviations of D_n from D_{CJ} are $\mathcal{O}(1)$, specifically

$$B\kappa_s = 1 - \cos\phi + \mathcal{O}(\epsilon), \quad D_n = D_{CJ}\cos\phi + \mathcal{O}(\epsilon). \tag{4.9}$$

A composite solution can be derived for $r(\phi)/B$ as

$$\frac{r}{B} = \sqrt{\frac{2}{\epsilon}}\tan^{-1}\left(\frac{\phi}{\sqrt{2\epsilon}}\right) - \phi - \frac{1}{\tan(\phi/2)} + \frac{2}{\phi}, \tag{4.10}$$

while for $z(\phi)/B$,

$$\frac{z}{B} = -\ln(1 - \cos\phi) - \ln\left[2 + \frac{\phi^2}{\epsilon}\right] + 2\ln\phi. \tag{4.11}$$

4.2. Rate-stick Geometry

For the rate-stick geometry, the differential equation (3.6) for $r(\phi)/B$ becomes

$$\left[1 - (1 - \epsilon)\cos\phi - \frac{\sin\phi}{(r/B)}\right]\frac{d(r/B)}{d\phi} = \cos\phi. \tag{4.12}$$

We again find an inner layer in the central part of the charge where $\phi = \mathcal{O}(\sqrt{\epsilon})$ and $r/B = \mathcal{O}(1/\sqrt{\epsilon})$. Defining

$$\hat{\phi} = \frac{\phi}{\sqrt{\epsilon}}, \quad \frac{\hat{r}}{B} = \frac{\sqrt{\epsilon}r}{B}, \quad \frac{\hat{r}}{B} \sim \frac{\hat{r}_0}{B} + \mathcal{O}(\epsilon), \tag{4.13}$$

and using (4.12), the equation governing $\hat{r}_0/B$ is given by

$$\left(1 + \frac{\hat{\phi}^2}{2} - \frac{\hat{\phi}}{(\hat{r}_0/B)}\right)\frac{d(\hat{r}_0/B)}{d\hat{\phi}} = 1. \tag{4.14}$$

The solution is

$$\hat{\phi} = \frac{\sqrt{2}J_1(\hat{r}_0/\sqrt{2}B)}{J_0(\hat{r}_0/\sqrt{2}B)}, \tag{4.15}$$

where J_0 and J_1 are the order zero and order one Bessel functions of the first kind. In this layer, the scaled curvatures $B\kappa_s = \mathcal{O}(\epsilon)$ and $B\kappa_a = \mathcal{O}(\epsilon)$, while deviations of D_n from D_{CJ} are $\mathcal{O}(\epsilon)$. Specifically in terms of ϕ,

$$B\kappa_s \sim -\epsilon\frac{(\phi/\sqrt{\epsilon})}{(\hat{r}_0/B)} + \epsilon\left(1 + \frac{\phi^2}{2\epsilon}\right), \quad B\kappa_a \sim \epsilon\frac{(\phi/\sqrt{\epsilon})}{(\hat{r}_0/B)},$$

$$D_n \sim D_{CJ}\left[1 - \epsilon\left(1 + \frac{\phi^2}{2\epsilon}\right)\right]. \tag{4.16}$$

As for the slab geometry, contained within the inner layer is a region near $r = 0$ where $\phi = \mathcal{O}(\epsilon)$, in which

$$\frac{r}{B} \sim \frac{2\phi}{\epsilon}, \quad B\kappa_s \sim \frac{\epsilon}{2}, \quad B\kappa_a \sim \frac{\epsilon}{2}, \quad D_0 \sim D_{CJ}(1 - \epsilon). \tag{4.17}$$

For $\phi_{edge} = \mathcal{O}(1)$, we must again insert an outer layer which extends to the edge of the charge. As for the slab geometry, $\phi = \mathcal{O}(1)$ and $r/B = \mathcal{O}(1/\sqrt{\epsilon})$. With these scalings, the axisymmetric curvature component is

$$B\kappa_a = \frac{\sin \phi}{(r/B)} = \mathcal{O}(\sqrt{\epsilon}), \tag{4.18}$$

and thus up to $\mathcal{O}(\sqrt{\epsilon})$ the rate-stick solution describing the variation of r/B with ϕ has a similar form to the slab solution in the outer layer. Matching with the inner layer gives

$$\frac{r}{B} = \frac{\sqrt{2}\beta}{\sqrt{\epsilon}} - \phi - \frac{1}{\tan(\phi/2)} + \mathcal{O}(\sqrt{\epsilon}), \tag{4.19}$$

where $\beta \approx 2.40483$ is the first positive zero of $J_0(\beta) = 0$. In the outer layer, the scaled slab curvature component $B\kappa_s = \mathcal{O}(1)$, the scaled axisymmetric component $B\kappa_a = \mathcal{O}(\sqrt{\epsilon})$, while deviations of D_n from D_{CJ} are $\mathcal{O}(1)$, specifically

$$B\kappa_s = 1 - \cos \phi + \mathcal{O}(\sqrt{\epsilon}), \quad D_n = D_{CJ} \cos \phi + \mathcal{O}(\epsilon). \tag{4.20}$$

A composite solution can be written as

$$\frac{r}{B} = \frac{r_0(\phi)}{B} - \phi - \frac{1}{\tan(\phi/2)} + \frac{2}{\phi}, \tag{4.21}$$

where r_0/B is the solution to

$$\frac{\phi}{\sqrt{\epsilon}} = \frac{\sqrt{2}J_1(\sqrt{\epsilon}r_0/\sqrt{2}B)}{J_0(\sqrt{\epsilon}r_0/\sqrt{2}B)}. \tag{4.22}$$

Also for the rate-stick, the differential equation (3.6) for $z(\phi)/B$ is

$$\left[1 - (1 - \epsilon)\cos \phi - \frac{\sin \phi}{(r/B)}\right]\frac{d(z/B)}{d\phi} = -\sin \phi, \text{ or } \frac{d(z/B)}{d(r/B)} = -\tan \phi. \tag{4.23}$$

In the inner layer, where $\phi = \mathcal{O}(\sqrt{\epsilon})$, $r/B = \mathcal{O}(1/\sqrt{\epsilon})$ and $z/B = \mathcal{O}(1)$, we find to leading-order,

$$\frac{z}{B} \sim 2\ln\left[J_0\left(\frac{\sqrt{\epsilon}r_0}{\sqrt{2}B}\right)\right], \tag{4.24}$$

where $r_0(\phi)/B$ is again the solution to (4.22). Contained within this inner layer is a region near $z = 0$ where $\phi = \mathcal{O}(\epsilon)$, in which

$$\frac{z}{B} \sim -\frac{\phi^2}{\epsilon}. \tag{4.25}$$

In the outer layer, where $\phi = \mathcal{O}(1)$, $r/B = \mathcal{O}(1/\sqrt{\epsilon})$ and $z/B = \mathcal{O}(1)$, we find after matching with (4.24),

$$\frac{z}{B} \sim -\ln(1/\epsilon) + 2\ln[J_1(\beta)] - \ln(1 - \cos \phi). \tag{4.26}$$

A composite solution can be written as

$$\frac{z}{B} = -\ln(1 - \cos \phi) + 2\ln\left[\frac{\phi}{\sqrt{2}}J_0\left(\frac{\sqrt{\epsilon}r_0}{\sqrt{2}B}\right)\right]. \tag{4.27}$$

4.3. *Scaling factors*

The asymptotic analysis above reveals three cases of interest for the scaling factor ratio R/T:

• Case 1: Strong confinement defined by $\phi_{edge} = \mathcal{O}(\epsilon)$.

In this case, there is a single layer describing the solution for $0 \leqslant \phi \leqslant \phi_{edge}$, given by (4.7) for the slab geometry and (4.17) for the rate-stick geometry. Relative to the length-scale B, the rate-stick diameter and slab height are both $\mathcal{O}(1)$. In the rate-stick, the $\mathcal{O}(\epsilon)$ slab $B\kappa_s$ and axisymmetric $B\kappa_a$ components of curvature are equal across the charge, i.e. $\kappa_s/\kappa_a \sim 1$ for $0 \leqslant \phi \leqslant \phi_{edge}$. It then follows from (4.7) and (4.17) that

$$1 - R/T = \mathcal{O}(\epsilon) > 0, \tag{4.28}$$

i.e. the scale factor is unity to leading-order for strong confinement defined by $\phi_{edge} = \mathcal{O}(\epsilon)$. Specifically, to $\mathcal{O}(\epsilon)$, it can be shown that $R/T \sim 1 - \phi^2/12\epsilon$.

• Case 2: Moderately strong confinement defined by $\phi_{edge} = \mathcal{O}(\sqrt{\epsilon})$.

In this case, there is again a single layer describing the solution for $0 \leqslant \phi \leqslant \phi_{edge}$, given by (4.5) for the slab geometry and by (4.22) for the rate-stick geometry. Relative to the length-scale B, the rate-stick diameter and slab height are both $\mathcal{O}(1/\sqrt{\epsilon})$. In the rate-stick, the scaled slab and axisymmetric curvature components are again of size $\mathcal{O}(\epsilon)$. However, in a region of this layer defined by $\mathcal{O}(\epsilon) < \phi \leqslant \phi_{edge}$, the two curvature components are no longer equal. Moreover, $\kappa_s/\kappa_a > 1$ (4.16) with the ratio κ_s/κ_a increasing as ϕ increases. The fact that the curvature components are different in the region $\mathcal{O}(\epsilon) < \phi \leqslant \phi_{edge}$ drives the scale factor below unity by $\mathcal{O}(1)$ amounts, i.e.

$$1 - R/T = \mathcal{O}(1) > 0, \tag{4.29}$$

for moderately strong confinement defined by $\phi_{edge} = \mathcal{O}(\sqrt{\epsilon})$. The actual value of the ratio R/T is determined through (4.5) and (4.22).

• Case 3: Weak or no confinement defined by $\phi_{edge} = \mathcal{O}(1)$.

In this case, the solution for $0 \leqslant \phi \leqslant \phi_{edge}$ is now described by two layers. The inner layer, represented by case 2 above, for $\phi = \mathcal{O}(\sqrt{\epsilon})$, is joined to an outer layer where $\phi = \mathcal{O}(1)$. Relative to the length-scale B, the rate-stick diameter and slab height are again both $\mathcal{O}(1/\sqrt{\epsilon})$. The composite solutions for $0 \leqslant \phi \leqslant \phi_{edge}$ when $\phi_{edge} = \mathcal{O}(1)$ are given by (4.10) and (4.21). Significantly, in the outer layer, the curvature is dominated by the slab component where $B\kappa_s = \mathcal{O}(1)$ while $B\kappa_a = \mathcal{O}(\sqrt{\epsilon})$. The outer layer solutions (4.8) and (4.19) describing the extent of the slab and rate-stick charge size when $\phi_{edge} = \mathcal{O}(1)$ show that in both cases the charge extent becomes independent of ϕ to leading-order. Consequently, the scaling factor ratio R/T is constant to leading-order. Specifically, we find that

$$R/T = \frac{\beta}{\pi} + \mathcal{O}(\epsilon), \tag{4.30}$$

where $\beta/\pi \approx 0.7655$, for weak or no confinement defined by $\phi_{edge} = \mathcal{O}(1)$. The specific value of the edge confinement angle influences the scaling factor ratio at $\mathcal{O}(\epsilon)$.

Figure 22 shows the variation of slab thickness and the rate-stick radius as a function of ϕ for the linear $D_n - \kappa$ law (4.1) with parameters $B = 0.1$ cm and $D_{CJ} = 0.775525188$ cm/μs (this D_{CJ} is the PBX 9502 value from table 9) at a fixed phase velocity of $D_0 = 0.775$ cm/μs ($\epsilon = 6.772 \times 10^{-4}$), calculated with the composite solutions (4.10) and (4.21) and also numerical solutions of (3.6) for the slab and rate-stick geometries. The agreement between the asymptotic and numerical solutions is excellent. Figure 23 shows the corresponding variation with z of ϕ from the rate-stick geometry and $2z$ from the slab geometry. The factor of 2 in the slab geometry ensures that the ratio
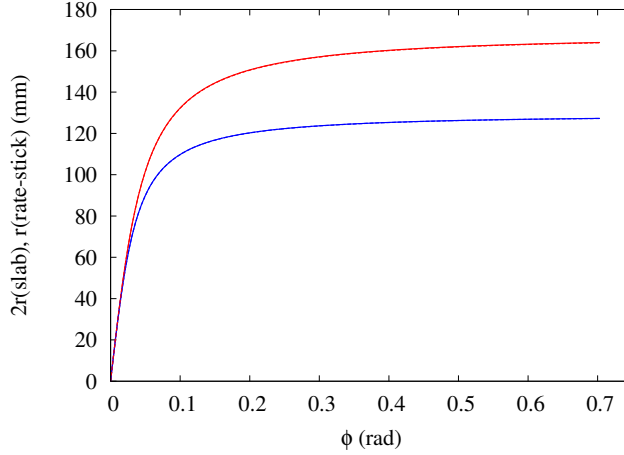
FIGURE 22. Comparison of the composite solutions (4.10) and (4.21) (dashed lines) with numerical solutions of (3.6) (solid lines) for slab thickness (red lines) and rate-stick radius (blue lines) as a function of ϕ. Here $B = 0.1$ cm and $D_{CJ} = 0.775525188$ cm/μs at a fixed phase velocity of $D_0 = 0.775$ cm/μs ($\epsilon = 6.772 \times 10^{-4}$). The corresponding composite and numerical solutions overlay in the plot.
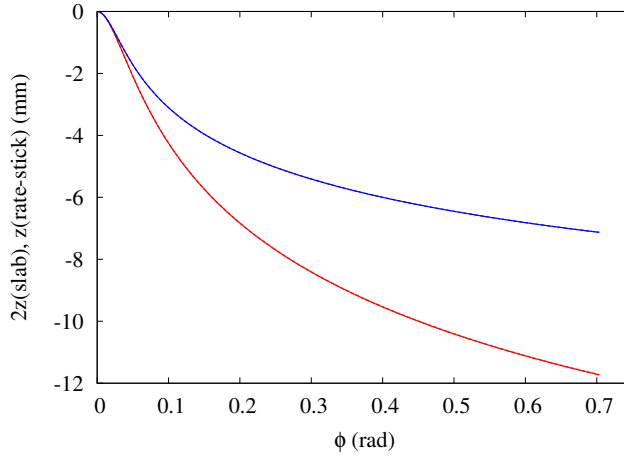

FIGURE 23. Comparison of the variation with z of ϕ from the rate-stick geometry (blue lines) and $2z$ from the slab geometry (red lines) corresponding to figure 22 for composite solutions (4.11) and (4.27) (dashed lines) and numerical solutions of (3.6) (solid lines). Again, the corresponding composite and numerical solutions overlay in the plot.

z(rate-stick)$/2z$(slab) ~ 1 in the layer where $\phi = \mathcal{O}(\epsilon)$ based on (4.7) and (4.25). Again the agreement between the composite solutions (4.11) and (4.27) with numerical solutions of (3.6) is excellent.

Figure 24 shows a comparison of the scale factor variation R/T with ϕ derived from composite solutions (4.10) and (4.21) (dashed line) and from numerical solutions of (3.6) (solid lines). A rapid decrease in the ratio of R/T is observed for small ϕ before approaching close to the limit defined by (4.30). Figure 25 shows the corresponding variation in the ratio of z from the rate-stick geometry and $2z$ from the slab geometry for composite solutions (4.11) and (4.27) and a numerical solution of (3.6). A rapid drop in the ratio is observed for small ϕ before decreasing more slowly for larger ϕ. Note
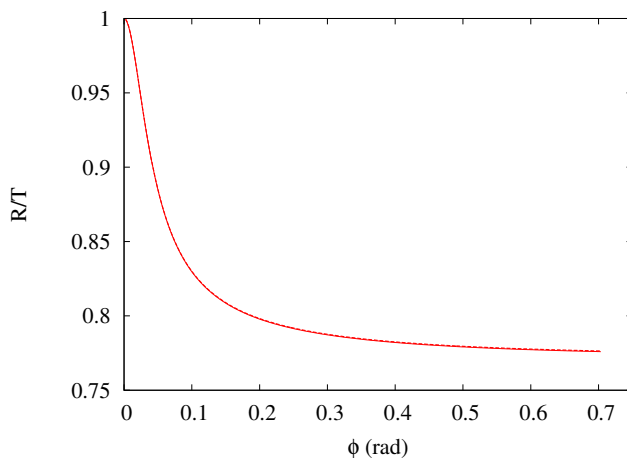
FIGURE 24. Comparison of the scale factor variation R/T with ϕ derived from composite solutions (4.10) and (4.21) (dashed line) and from numerical solutions of (3.6) (solid lines). Here $B = 0.1$ cm and $D_{CJ} = 0.775525188$ cm/μs at a fixed phase velocity of $D_0 = 0.775$ cm/μs ($\epsilon = 6.772 \times 10^{-4}$). The composite and numerical solutions almost overlay in the plot.
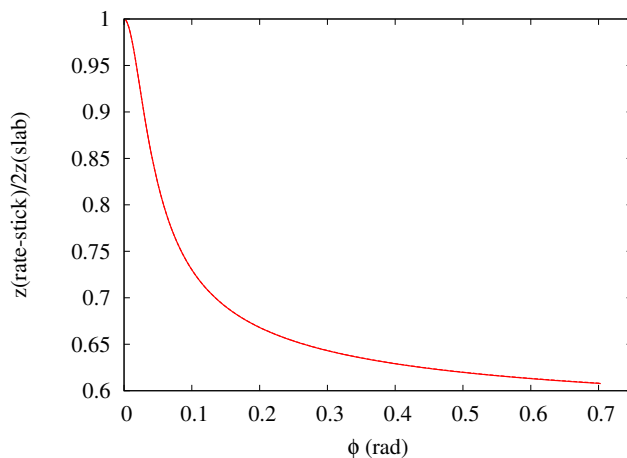

FIGURE 25. Comparison of the variation with ϕ of the ratio of z from the rate-stick geometry and 2z from the slab geometry corresponding to figure 24 for composite solutions (4.11) and (4.27) (dashed lines) and a numerical solution of (3.6) (solid lines). Again, the composite and numerical solutions overlay in the plot.

that for sufficiently small ϵ the outer layer solutions for z, (4.8) and (4.26), indicate z(rate-stick)$/2z$(slab) $\sim 1/2$ when $\phi_{edge} = \mathcal{O}(1)$. In both figures, the agreement between the asymptotic and numerical solutions is excellent.

Figure 26 shows a comparison of the scale factor R/T variation with D_0 derived from the composite solutions (4.10) and (4.21) and a numerical solution of (3.6) for an $\mathcal{O}(1)$ edge angle $\phi_{edge} = 0.7033841$. For small ϵ, the composite and numerical solutions are in good agreement. As ϵ increases, the solutions diverge, but the asymptotic solutions still provide a reasonable approximation to the numerical solution even at values of D_0 significantly below D_{CJ} (at $D_0 = 7$ mm/μs, $\epsilon = 0.0974$).
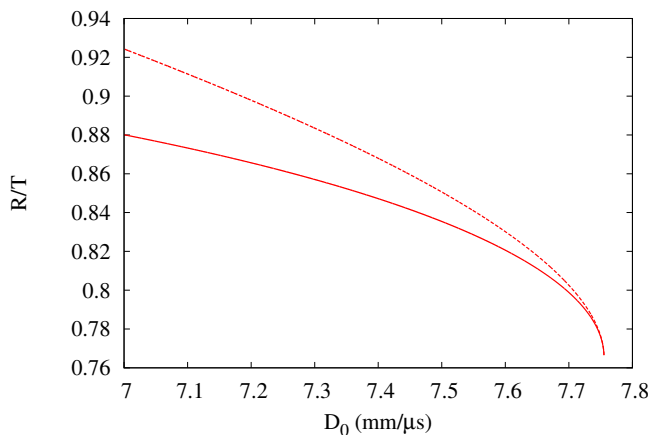
FIGURE 26. Scale factor R/T variation with changes in D_0 with $B = 0.1$ cm and $D_{CJ} = 0.775525188$ cm/μs for an edge angle $\phi_{edge} = 0.7033841$. A composite solution from (4.10) and (4.21) (dashed line) and numerical solution of (3.6) (solid line) are shown.

5. Summary

The detonation-velocity thickness-effect curves were experimentally measured for ideal (PBX 9501), insensitive (PBX 9502) and non-ideal (ANFO) high explosives by propagating detonation in a rectangular slab geometry. These data allowed examination of the geometric scaling factor $R(D_0)/T(D_0)$ when compared to previous diameter-effect data obtained from a cylindrical rate-stick geometry. The diameter- and thickness-effect data yielded a varying scaling value that was always such that $R(D_0)/T(D_0) < 1$ for all explosives studied.

For PBX 9501 and PBX 9502, the lower-order form of the Detonation Shock Dynamics (DSD) model was found to provide a good approximation to the observed $R(D_0)/T(D_0) < 1$ behavior, and explains why, due to the difference in slab and axisymmetric components of curvature in the rate-stick configuration, a curvature-based theory should in general predict a scaling different from $R(D_0)/T(D_0) = 1$. For the non-ideal explosive ANFO, the lower-order DSD model did not reproduce the observed $R(D_0)/T(D_0)$ scaling. A higher-order DSD theory, which includes contributions due to detonation front acceleration and transverse flow was found to be required to reproduce the experimental scaling. An asymptotic analysis of the lower-order DSD model provided insights into the behavior of the geometrical scaling factor $R(D_0)/T(D_0)$ when the detonation phase velocity approaches the Chapman-Jouguet detonation velocity. Three cases were identified for different degrees of explosive confinement, yielding $R(D_0)/T(D_0)$ values that increasingly descended from a near unity value with increasing charge edge angle, limiting to a constant value for $\mathcal{O}(1)$ edge angles.

Comparison of diameter- and thickness-effect curves provide fundamental validation on the predictive capability of detonation models such as DSD when the model calibration is conducted using data from one geometry, and then used to predict detonation velocity effect curves in a different geometry. The thickness-effect data indicated that improved DSD model calibrations are needed for ANFO and low velocity PBX 9501 detonation.

6. Acknowledgements

REFERENCES

ANDERSON, E.K., ASLAM, T.D. & JACKSON, S.I. 2014 Transverse initiation of an insensitive explosive in a layered slab geometry: Front shapes and post-shock flow measurements. *In press with Combustion and Flame* **161**.

ASLAM, T.D. 2007 Detonation shock dynamics calibration of PBX 9501. In *Shock Compression of Condensed Matter* (ed. M. Elert, M.D. Furnish, R. Chau, N. Holmes & J. Nguyen), *CP* 955, pp. 813–816. American Institute of Physics.

ASLAM, T.D., BDZIL, J.B. & HILL, L.G. 1998 Extensions to DSD theory: Analysis of PBX 9502 rate tick data. In *Eleventh (International) Detonation Symposium*, pp. 21–29. Office of Naval Research, ONR 33300-2.

ASLAM, T., JACKSON, S.I. & MORRIS, J.S. 2009 Proton radiography of PBX 9502 detonation shock dynamics confinement sandwich test. In *Shock Compression of Condensed Matter* (ed. M.L. Elert, W.T. Buttler, M.D. Furnish, W.W. Anderson & W.G. Proud), *CP* 1195, pp. 241–244. American Institute of Physics.

ASLAM, T.D. & STEWART, D.S. 1999 Detonation shock dynamics and comparisons with direct numerical simulations. *Combust. Theory Modell.* **3**, 77–101.

BDZIL, J.B. 1981 Steady-state two-dimensional detonation. *J. Fluid Mech.* **108**, 195–226.

BDZIL, J.B. 2003 Detonation shock dynamics calibration for PBX 9502. Private communication.

BDZIL, J.B. 2008 Detonation shock dynamics calibration for ANFO. Private communication.

BDZIL, J.B., ASLAM, T.D., CATANACH, R.A., HILL, L.G. & SHORT, M. 2002 DSD front models: Nonideal explosive detonation in ANFO. In *Twelfth International Detonation Symposium*, pp. 409–417. Office of Naval Research, ONR 333-05-2.

BDZIL, J.B., ASLAM, T.D., HENNINGER, R. & QUIRK, J.J. 2003 High-explosives performance - Understanding the effects of a finite-length reaction zone. *Los Alamos Science* **28**, 96–110.

BDZIL, J.B. & DAVIS, W.C. 1975 Time-dependent detonations. *Tech. Rep.* LA-5926-MS. Los Alamos National Laboratory.

BDZIL, J.B., FICKETT, W. & STEWART, D. S. 1989 Detonation shock dynamics: A new approach to modeling multi-dimensional detonation waves. In *Ninth Symposium (International) on Detonation*, pp. 730–742. Office of the Chief of Naval Research, OCNR 113291-7.

BDZIL, J.B., SHORT, M., SHARPE, G.J., ASLAM, T.D. & QUIRK, J.J. 2006 Higher-order DSD for detonation propagation: DSD for detonation driven by multi-step chemistry models with disparate rates. In *Thirteenth International Detonation Symposium*, pp. 726–736. Office of Naval Research, ONR 351-07-01.

BDZIL, J.B. & STEWART, D.S. 1986 Time-dependent two-dimensional detonation: the interaction of edge rarefactions with finite-length reaction zones. *J. Fluid Mech.* **171**, 1–26.

BDZIL, J.B. & STEWART, D.S. 1989 Modelling two-dimensional detonations with detonation shock dynamics. *Phys. Fluids A* **1**, 1261–1267.

BDZIL, J.B. & STEWART, D.S. 2007 The dynamics of detonation in explosive systems. *Ann. Rev. Fluid Mech.* **39**, 263–292.

BRUN, L., KNEIB, J.M. & LASCAUX, P. 1994 Computing the transient self-sustained detonation after a new model. In *Tenth International Detonation Symposium*, pp. 43–49. Office of Naval Research, ONR.

CAMPBELL, A.W & ENGELKE, R 1976 The diameter effect in high-density heterogeneous explosives. In *Sixth Symposium (International) on Detonation*, pp. 642–652. Office of Naval Research ACR-221.

CHIQUETE, C., JACKSON, S.I. & SHORT, M. 2014 DSD calibration of PBX 9501 via slab geometry experiments. In *Fifthteenth International Detonation Symposium*. Office of Naval Research, to appear.

COLLYER, A.M., DUNNETT, J.D., SWIFT, D.C. & WHITE, S.J. 1998 WBL detonation wave

propagation for EDC35 and EDC37. In *Eleventh International Detonation Symposium*, pp. 12–20. Office of Naval Research, ONR 33300-5.

EDEN, G. & BELCHER, R.A. 1989 The effects of inert walls on the velocity of detonation in EDC35, an insensitive high explosive. In *Ninth Symposium (International) on Detonation*, pp. 831–841. Office of the Chief of Naval Research, OCNR 113291-7.

EDEN, G. & WRIGHT, P.W. 1965 A technique for the precise measurement of the motion of a plane free surface. In *Fourth Symposium (International) on Detonation*, pp. 573–583. Office of Naval Research, ACR-126.

ENGELKE, R. & BDZIL, J.B. 1983 A study of the steady-state reaction-zone structure of a homogenous and a heterogenous explosive. *Phys. Fluids* **26**, 1210–1221.

GIBBS, T.R. & POPOLATO, A. 1980 *LASL Explosive Property Data*. University of California Press.

GOIS, C., PRESLES, H.N. & VIDAL, P. 1991 Effect of hollow heterogenities on nitromethane detonation. In *Dynamic Aspects of Detonations* (ed. A.L. Kuhl, J.-C. Leyer, A.A. Borisov & W.A. Sirignano), *Progress in Aeronautics and Astronautics* 153, pp. 462–470.

GOIS, J.C., CAMPOS, J. & MENDES, R. 1996 Extinction and initiation of detonation of NM-PMMA-GMB mixtures. In *Shock Compression of Condensed Matter* (ed. S.C Schmidt & W.C. Tao), *CP* 370, pp. 827–830. American Institute of Physics.

HELM, F, FINGER, M, HAYES, B, LEE, E, CHEUNG, H & WALTON, J 1976 High explosive characterization for the dice throw event. *Tech. Rep.* UCRL-52042. Lawrence Livermore Laboratory.

HIGGINS, A. 2009 Measurement of detonation velocity for a nonideal heterogenous explosive in axisymmetric and two-dimensional geometries. In *Shock Compression of Condensed Matter* (ed. M.L. Elert, W.T. Buttler, M.D. Furnish, W.W. Anderson & W.G. Proud), *CP* 1195, pp. 193–196. American Institute of Physics.

HILL, L.G. & ASLAM, T.D. 2004 The LANL detonation-confinement test: Prototype development and sample results. In *Shock Compression of Condensed Matter* (ed. M.D. Furnish, Y.M. Gupta & J.W. Forbes), *CP* 706, pp. 847–850. American Institute of Physics.

HILL, L.G. & ASLAM, T.D. 2010 Detonation shock dynamics calibration for PBX 9502 with temperature, density, and material lot variations. In *Fourteenth International Detonation Symposium*, pp. 779–788. Office of Naval Research, ONR-351-10-185.

HILL, L.G., BDZIL, J.B., DAVIS, W.C. & CRITCHFIELD, R.R. 2006 PBX 9502 front curvature rate stick data: Repeatability and the effects of temperature and material variation. In *Thirteenth International Detonation Symposium*, pp. 331–341. Office of Naval Research, ONR 351-07-01.

HILL, L. G. 2012 Compilation of ambient PBX 9501 detonation speed data. *Tech. Rep.*. Los Alamos National Laboratory.

JACKSON, S.I., AUSTIN, J.M. & SHEPHERD, J.E. 2006 Planar detonation wave initiation in large-aspect-ratio channels. *AIAA Journal* **44** (10), 2422–2425.

JACKSON, S.I., KIYANDA, C.B. & SHORT, M. 2011 Experimental observations of detonation in ammonium-nitrate-fuel-oil (ANFO) surrounded by a high-sound-speed, shockless, aluminum confiner. *Proceedings of the Combustion Institute* **33**, 2219–2226.

JACKSON, S.I. & SHORT, M. 2012 Determination of the velocity-curvature relationship for unknown front shapes. In *Shock Compression of Condensed Matter* (ed. M.L. Elert, W.T. Buttler, J.P. Borg, J.L. Jordan & T.J. Vogler), *CP* 1426, pp. 347–350. American Institute of Physics.

KASIMOV, A.R. & STEWART, D.S. 2005 Asymptotic theory of evolution and failure of self-sustained detonations. *J. Fluid Mech.* **525**, 161–192.

KENNEDY, D.L. 1998 Multi-valued normal shock velocity versus curvature relationships for highly non-ideal explosives. In *Eleventh (International) Detonation Symposium*, pp. 181–192. Office of Naval Research, ONR 33300-2.

KENNEDY, J.E. 1997 The gurney model of explosive output for driving metal. In *Explosive Effects and Applications* (ed. J.A. Zukas & W.P. Walters), pp. 221–257. Springer-Verlag New York.

MACK, D.B., PETEL, O.E. & HIGGINS, A.J. 2007 Detonation failure thickness measurement in an annular geometry. In *Shock Compression of Condensed Matter* (ed. M. Elert, M.D.

Furnish, R. Chau, N. Holmes & J. Nguyen), *CP* 955, pp. 833–836. American Institute of Physics.

MORRIS, J.S., JACKSON, S.I. & HILL, L.G. 2009 A simple line wave generator using commercial explosives. In *Shock Compression of Condensed Matter* (ed. M.L. Elert, W.T. Buttler, M.D. Furnish, W.W. Anderson & W.G. Proud), *CP* 1195, pp. 408–411. American Institute of Physics.

PETEL, O.E. & HIGGINS, A.J. 2006 Comparison of failure thickness and critical diameter of nitromethane. In *Shock Compression of Condensed Matter* (ed. M.D. Furnish, M. Elert, T.P. Russell & C.T. White), *CP* 845, pp. 994–997. American Institute of Physics.

PETEL, O.E., MACK, D., HIGGINS, A.J., TURCOTTE, R. & CHAN, S.K. 2006 Comparison of the detonation failure mechanism in homogenous and heterogenous explosives. In *Thirteenth International Detonation Symposium*, pp. 2–11. Office of Naval Research, ONR 351-07-01.

PETEL, O.E., MACK, D., HIGGINS, A.J., TURCOTTE, R. & CHAN, S.K. 2007 Minimum propagation diameter and thickness of high explosives. *Journal of Loss Prevention in the Process Industries* **20**, 578–583.

RAMSAY, J. 1985 Effect of confinement on failure in 95 TATB/5 Kel-F. In *Eighth Symposium (International) on Detonation*, pp. 372–379. Naval Surface Weapons Center, NSWC MP 86-194.

SHARPE, G.J. & BDZIL, J.B. 2006 Interactions of inert confiners with explosives. *Journal of Engineering Mathematics* **54** (3), 273–298.

SHORT, M. & JACKSON, S.I. 2015 Dynamics of high sound-speed metal confiners driven by non-ideal high-explosive detonation. *In press with Combustion and Flame* .

SHORT, M., QUIRK, J.J., KIYANDA, C.K., JACKSON, S.I., BRIGGS, M.E. & SHINAS, M.A. 2010 Simulation of detonation of ammonium nitrate fuel oil mixture confined by aluminium: Edge angles for DSD. In *Fourteenth International Detonation Symposium*, pp. 769–778. Office of Naval Research, ONR-351-10-185.

SILVESTROV, V. V., PLASTININ, A. V., KARAKHANOV, S. M. & ZYKOV, V. V. 2008 Critical diameter and critical thickness of an emulsion explosive. *Combustion, Explosion, and Shock Waves* **44** (3), 354–359.

STEWART, D.S. & BDZIL, J.B. 1988*a* A lecture on detonation-shock dynamics. In *Mathematical Modeling in Combustion Science* (ed. J.D. Buckmaster & T. Takeno), *Lecture Notes in Physics*, vol. 299, pp. 17–30. Springer Berlin Heidelberg.

STEWART, D.S. & BDZIL, J.B. 1988*b* The shock dynamics of stable multidimensional detonation. *Combustion and Flame* **72**, 311–323.

YAO, J. & STEWART, D.S. 1996 On the dynamics of multi-dimensional detonation. *J. Fluid Mech.* **309**, 225–275.

YOSHINAKA, A. & ZHANG, F. 2004 Shock initiation and detonability of liquid nitroethane. In *Shock Compression of Condensed Matter* (ed. M.D. Furnish, Y.M. Gupta & J.W. Forbes), *CP* 706, pp. 1069–1072. American Institute of Physics.